Multiresolution-based grid adaptation for the compression of ERA5 meteorological reanalysis data in MPTRAC v2.7

Farahnaz Khosrawi[1], Adrian Kolb[2], Lars Hoffmann[1], and Siegfried Müller[2]

[1]Jülich Supercomputing Centre, Forschungszentrum Jülich, Jülich, Germany
[2]Institut für Geometrie und praktische Mathematik, RWTH Aachen, Aachen, Germany

Correspondence: Farahnaz Khosrawi (f.khosrawi@fz-juelich.de)

Abstract. The continuous increase in computational power comes with a corresponding demand for storage space. However, the ability to store data has hardly increased in recent years. This makes the demand for efficient storage solutions even more pressing, especially for meteorological reanalysis data. The current European Centre for Medium-Range Weather Forecasts (ECMWF) ERA5 reanalysis data already poses a major challenge for the community, but with the upcoming ERA6 reanalysis data, which will have an even higher resolution, significantly more storage space will be needed. An efficient way to store data is to use either lossy or lossless data compression methods to reduce storage requirements. To compress the meteorological data, we perform a multiresolution-analysis using multiwavelets on a hierarchy of nested grids. Since the local differences become negligibly small in regions where the data are locally smooth, we apply hard thresholding for data compression. This results in a high compression rate while preserving the accuracy of the original data. This strategy has been implemented into the Lagrangian model for Massive-Parallel Trajectory Calculation (MPTRAC) and has been successfully applied to ERA5 reanalysis data. Compression rates ranging from 1.6 to 12.6 can be achieved while at the same time maintaining the accuracy of the data within acceptable error limits. This leads to a reduction in storage of up to 93%, for example, reducing the file size of an ERA5 data file corresponding to a time instant from 4.9 GB to 389 MB. This renders the multiresolution-based grid adaptation a particularly suitable and effective approach for addressing the data storage challenges in atmospheric transport simulations.

1 Introduction

Supercomputing resources have significantly increased in recent years, allowing atmospheric modellers to run their global simulations with very high resolution. However, this comes with an immense demand for disk space, which, unfortunately, has not increased as rapidly as computing resources. One of the data sets used by many atmospheric modellers, e.g. to drive atmospheric model simulations, is the ECMWF ERA5 reanalysis (Hersbach et al., 2020). The current version of the reanalysis data already poses a challenge due to its large size, which has increased by a factor of about 80 compared to its predecessor

ERA-Interim (Hoffmann et al., 2019). Using the ECMWF data sets will become even more challenging when the new ERA6 version is released.

ECMWF usually provides the data in the GRIB (General Regularly-distributed Information in Binary form) format. GRIB is a data format developed by the World Meteorological Organization (World Meteorological Organization, 2025). This data format is primarily used to encode the results from weather forecast models. GRIB is a tabular format that is written in binary format and has been designed to transfer, store and process data efficiently. Since GRIB has been developed for machine processing, additional software is required to handle the data. This makes the usage for the atmospheric science community somewhat cumbersome and, thus, usually the data are converted into the Network Common Data Form (NetCDF) for further handling. This format also has nowadays become a community standard for sharing scientific data. NetCDF is a set of software libraries and machine-independent data formats that support the creation, access, and sharing of array-oriented scientific data. The Unidata Program Center supports and maintains NetCDF programming interfaces for several common programming languages as C, C++, Java, and Fortran and interfaces for programming languages as Python, IDL, or MATLAB that are used for graphical processing of the data (https://www.unidata.ucar.edu/software/netcdf/). A way to overcome the problem with the immense demand for disk space is to compress the data. A detailed overview of currently available compression methods is provided in Duwe et al. (2020). Both NetCDF and GRIB provide lossless and lossy compression methods. However, lossless compression techniques rarely achieve more than 1.5× compression on double-precision data (Lindstrom, 2014). Thus, for achieving a significant reduction in file size lossy compression techniques are required (Klöwer et al., 2021).

Several new lossless and lossy compression methods have been developed in the past decade. Examples for conventional lossless compression methods that are public, reliable and widely used are e.g. bzip2 and gzip (Walters and Wong, 2023). A more advanced lossless compression method, which is similar to gzip (https://datatracker.ietf.org/doc/html/rfc1952), is ZStandard (ZSTD, https://datatracker.ietf.org/doc/html/rfc8878). In order to be as flexible as with NetCDF4 and HDF5 and improving the compression that is typically achieved with these so that they are comparable to GRIB2, Silver and Zender (2017) introduced a new compression method called "layer-packing". Layer packing simultaneously exploits lossy linear scaling and lossless compression. Another example for a lossy compression method with which high compression ratios can be achieved is ZFP (Lindstrom, 2014). ZFP is a compression scheme for multi-dimensional double-precision and floating-point data and was inspired by ideas developed for texture compression of 2-D image data. For instance, using this compression scheme, a 3-D array is divided into small, fixed size blocks of dimensions 4×4×4 that are each stored using the same, user specified number of bits, and which can be accessed entirely independently. Similar modes are offered by the SZ compression method (Di and Cappello, 2016; Tao et al., 2017). SZ is a modular parameterizable lossy compressor framework for scientific floating point and integer data.

Recently, compression techniques based on machine learning techniques have been proposed (e.g. Huang and Hoefler, 2023; Liu et al., 2024). Additionally, adaptive mesh refinement, which has been used for atmospheric model simulations, such as climate simulations and Lagrangian transport modelling (e.g. Jablonowski et al., 2009; Garcia-Menendez and Odman, 2011; Gerwig et al., 2018; Chen et al., 2021), has been suggested as compression technique (Böing et al., 2024).

Previous studies that focused on the compression of data stored in the NetCDF file format were conducted by Zender (2016); Silver and Zender (2017) and Delaunay et al. (2019). Studies on the compression of ERA5 data, specifically, were done by Huang and Hoefler (2023) and Tintó Prims et al. (2024). Poppick et al. (2020) point out the importance of evaluating the quality of compression in order to ensure that minimal scientific information is lost due to compression. Evaluation of lossy compression of climate data was done by e.g. Baker et al. (2016); Poppick et al. (2020); Huang and Hoefler (2023) and Hübbe et al. (2013).

In this study we introduce an adaptive mesh refinement strategy for data compression, similar to Böing et al. (2024), but using a multiresolution-based grid adaptation. In Böing et al. (2024) each data point is mapped onto a single element of an initially fine grid and then adaptive coarsening is applied. For an indicator they develop a two-scale strategy that was originally introduced by Harten (1993, 1996). Harten's discrete concept of prediction and reconstruction corresponds one-to-one to wavelets (Gottschlich-Müller and Müller, 1999). Reinterpreted in the wavelet context, the Haar wavelet used in Böing et al. (2024) corresponds to piecewise constant data in each grid element. In the present study, this compression approach has been extended to piecewise polynomial data and multiwavelets, which is expected to give higher compression rates than Böing et al. (2024) due to higher vanishing moments.

The outline of the paper is as follows. In Sect. 2, we describe the ERA5 reanalysis dataset used in this work and present our novel approach to apply multiresolution analysis for lossy compression of meteorological data. We summarize the mathematical foundations and demonstrate that effective compression can be obtained by thresholding non-significant local details. The practical implementation is provided by the MRA-MW library, which performs multiresolution analysis on piecewise polynomial functions using multiwavelets. This library is integrated into the Lagrangian Model for Massive Parallel Trajectory Calculations (MPTRAC). Section 3 presents the results of the compression tests we performed with the compression method based on multiresolution analysis. We analyzed several test cases to assess how strong we can compress the ERA5 data and evaluate the quality of our compression by using the root mean square error (RMSE) and the Pearson correlation coefficient. In addition, we perform trajectory calculations with the Lagrangian Model for Massive Parallel Trajectory Calculations (MPTRAC) to test how data files compressed by multiresolution-based grid adaptation affect the trajectory calculations. To assess the accuracy of the trajectories we consider the absolute and relative horizontal and vertical transport deviations (Kuo et al., 1985; Stohl, 1998). Finally, we benchmark the presented method against alternative compression techniques. In Sect. 4, we conclude our results and provide an outlook.

2 Data and method

2.1 Meteorological data

2.1.1 ERA5

ERA5 is the fifth generation ECMWF atmospheric reanalysis of the global climate, produced by the Copernicus Climate Change Service (C3S) at ECMWF. ERA5 provides hourly estimates of a large number of atmospheric, land and oceanic climate variables over the period from January 1940 to present (Hersbach et al., 2020). The data have been retrieved from the ECMWF data server on a 0.3° × 0.3° (30 × 30 km) horizontal grid (T_L639) and 137 vertical levels covering the atmosphere from the ground to up to 0.01 hPa (about 80 km altitude) with a temporal resolution of 1 h. Meteorological variables that have been downloaded are the following: geopotential (z), temperature (T), specific humidity (q), vertical velocity (ω), surface pressure (sp), zonal wind (u), meridional wind (v), ozone (O_3), specific liquid cloud water content (SLWC), specific ice water content (CIWC), and various surface variables. The original ERA5 data have been retrieved in the GRIB format and then converted to NetCDF. The data are stored in hourly files (thus 24 files for one day) and each file has a size of 3.0 GB. After postprocessing with MPTRAC (Sect. 2.2.4), where additional meteorological variables are calculated and stored (e. g., geopotential heights and potential vorticity), the file size increases to 4.9 GB.

2.2 Data compression using multiresolution-based data analysis

In this work, we compress ERA5 reanalysis data using multiresolution analysis. For this purpose, we map the field of discrete data to a function. A multi-scale decomposition represents the function at successive levels of refinement, with detail coefficients quantifying differences between the levels. When the differences are small, the function can be projected onto a coarser grid without significant loss of information. Building on this principle, we construct an adaptive representation that preserves a prescribed accuracy while reducing the number of degrees of freedom. Storing the function in this adaptive multi-scale form yields an effective compression of the original set of discrete data.

2.2.1 Multiresolution-based data analysis

In the following, we present the main idea of the multiresolution-based data analysis. For a more detailed explanation of the multiresolution-based data analysis we refer to Gerhard (2017), Gerhard et al. (2015), and Gerhard and Müller (2016).

The starting point is a hierarchy of nested grids $\mathcal{G}_\ell := (V_\lambda)_{\lambda\in\mathcal{I}_\ell}$ defined on a domain $\Omega \subset \mathbb{R}^d$ where $\ell \in \mathbb{N}_0$ denotes the refinement level and $\mathcal{I}_\ell$ is the corresponding index set for the cells $V_\lambda \in \mathcal{G}_\ell$, $\lambda \in \mathcal{I}_\ell$. In this work, we only consider dyadic grid hierarchies using Cartesian grids. Unlike classical compression techniques that operate on discrete point values, the *multiresolution analysis* (MRA) acts on function spaces. To this end, we introduce a *discontinuous Galerkin* (DG) space

$$S_\ell := \{f \in L^2(V_\lambda) : f|_{V_\lambda} \in \Pi_{p-1}(V_\lambda), \lambda \in \mathcal{I}_\ell\}, \tag{1}$$

for each refinement level $\ell \in \mathbb{N}_0$. The DG space consists of piecewise polynomials $f|_{V_\lambda}$ in $\Pi_{p-1}(V_\lambda)$, with maximal degree $p-1$, for each cell $V_\lambda \in \mathcal{I}_\ell$. Here, $p \in \mathbb{N}$ denotes the *order* of the DG space. Using the DG space, a function $u^L \in S_L$ at the refinement level $L \in \mathbb{N}$ is represented by its *single-scale coefficients* on level $L \in \mathbb{N}$:

$$u^L := \sum_{\lambda\in\mathcal{I}_L} u^L_\lambda. \tag{2}$$

Here, the single-scale coefficients $u^L_\lambda \in S_L,\ \lambda \in \mathcal{I}_L$, are the projections of u onto S_L and are restricted to its corresponding cell $V_\lambda \in \mathcal{G}_L$.

Since the sequence of grids $(\mathcal{G}_\ell)_{\ell\in\mathbb{N}_0}$ is nested, it holds $S_\ell \subset S_{\ell+1}$ for all $\ell \in \mathbb{N}_0$. If, in addition, the sequence of nested grids $(\mathcal{G}_\ell)_{\ell\in\mathbb{N}_0}$ is dense in Ω, then the sequence of DG spaces $(S_\ell)_{\ell\in\mathbb{N}_0}$ forms a *multiresolution sequence* in $L^2(\Omega)$. Thus, for each level $\ell \in \mathbb{N}_0$ there exists an orthogonal space $W_\ell \subset S_{\ell+1}$ such that

$$S_{\ell+1} = S_\ell \oplus W_\ell. \tag{3}$$

We refer to W_ℓ as the *detail space*. The detail space provides information on the differences of a function u between successive refinement levels.

By applying recursively (3) to $u^L \in S_L$, $L \in \mathbb{N}$, we obtain its *multi-scale decomposition*

$$u^L = \sum_{\lambda\in\mathcal{I}_0} u_\lambda^0 + \sum_{\ell=0}^{L-1} \sum_{\lambda\in\mathcal{I}_\ell} d_\lambda^\ell, \tag{4}$$

where $u_\lambda^0 \in S^0$ is the projection of u onto S^0 and $d_\lambda^\ell \in W_\ell$ is the projection onto the detail spaces W_ℓ, $\ell \in \mathbb{N}_0$, restricted to V_λ with $\operatorname{supp}(d_\lambda^\ell) = V_\lambda$. The details d_λ^ℓ in the multi-scale decomposition (4) represent the local difference of the function between consecutive refinement levels. In particular, the details become small when the underlying data are locally smooth. This allows for local thresholding, i.e., if a local detail d_λ^ℓ on level $\ell \in \mathbb{N}_0$, $\lambda \in \mathcal{I}_\ell$ is sufficiently small, its local contribution to the function u may be considered negligible and is discarded. Therefore, we may project the function u^L on a coarser grid without significant loss of information. The compression rate increases with the polynomial degree. To formalize this, we define the set of significant details

$$\mathcal{D}_{\ell,\varepsilon} := \{\lambda \in \mathcal{I}_\ell : \|d_\lambda^\ell\|_{L^2(\Omega)} > \varepsilon_{\ell,\lambda}\}, \tag{5}$$

where $\varepsilon_{\ell,\lambda} > 0$ is a *local threshold value*. We refer to any local contribution $d_\lambda^\ell \in \mathcal{D}_{\ell,\varepsilon}$ as *significant*.

A *sparse approximation* $u^{L,\varepsilon}$ of the projection $u^L \in S_L$ is obtained by considering only its significant details (5):

$$u^{L,\varepsilon} := \sum_{\lambda\in\mathcal{I}_0} u_\lambda^0 + \sum_{\ell=0}^{L-1} \sum_{\lambda\in\mathcal{D}_{\ell,\varepsilon}} d_\lambda^\ell. \tag{6}$$

Additionally, we define the *global threshold value* $\varepsilon_{\max} > 0$ such that

$$\sum_{\ell=0}^{L-1} \max_{\lambda\in\mathcal{I}_\ell} \varepsilon_{\lambda,\ell} \leq \varepsilon_{\max}. \tag{7}$$

The key point of multiresolution-based grid adaptation is summarized in the following theorem:

Theorem 1 (Thresholding Error (Gerhard (2017); Gerhard and Müller (2016)))**.**
Let $\varepsilon_{max} > 0$ be a global threshold value and $\varepsilon_{\ell,\lambda} > 0$ be the local threshold values such that inequality (7) *holds. If the domain Ω is bounded then the threshold error of the sparse approximation* (6) *to the projection u^L* (4) *on level $L \in \mathbb{N}$ is bounded by*

$$\|u^L - u^{L,\varepsilon}\|_{L^2(\Omega)} \leq C \cdot \varepsilon_{max}. \tag{8}$$

The constant $C := \sqrt{|\Omega|} \cdot \sqrt{|\mathcal{P}|} \cdot \sqrt{|\mathcal{M}_\lambda| - 1} > 0$ is independent of the refinement level L and $\varepsilon_{\ell,\lambda}$.

The constant C depends on the size of the domain $|\Omega|$, the number of basis functions used for the DG space $|\mathcal{P}|$ and the number of children $\mathcal{M}_\lambda$ of a cell V_λ. Theorem 1 justifies discarding non-significant details from the projection u^L and locally projecting it onto a coarser grid while controlling the error introduced during the thresholding procedure. Due to the geometric sum, we choose the local threshold values in (7) as $\varepsilon_{\ell,\lambda} := h^{L-\ell} \cdot \varepsilon_{\text{max}}$, where $h > 0$ denotes the uniform cell diameter on the coarsest refinement level. A suitable choice of $\varepsilon_{\text{max}} > 0$ is crucial for determining the accuracy of the projection $u^{L,\varepsilon}$. Here, we set

$$\varepsilon_{\text{max}} := C_{\text{thresh}} \cdot h^L, \tag{9}$$

where $C_{\text{thresh}} > 0$ is a problem-dependent constant that acts as a filter. It can be set by the user to control which part of the data are refined more or are coarsened. The specific selection of this parameter in the context of ERA5 meteorological reanalysis data will be discussed in Sect. 2.2.2.

To obtain the DG representation corresponding to the sparse approximation (6), we perform a local inverse multi-scale transformation, providing us with the equivalent representation in terms of its single-scale coefficients:

$$u^{L,\varepsilon} = \sum_{\ell=0}^{L} \sum_{\lambda \in \mathcal{I}_{\ell,\varepsilon}} u_\lambda^\ell. \tag{10}$$

Here, $\{\mathcal{I}_{\ell,\varepsilon}\}_{\ell=0,\ldots,L}$ represents a local refined grid with $\{\mathcal{G}_{\ell,\varepsilon}\}_{\ell=0,\ldots L}$ containing cells on level $\ell = 0,\ldots,L$. Using the representation (10) of the sparse approximation on the DG space, rather than representation (6), enables efficient evaluation by simply evaluating the corresponding DG function. The adaptive grid is determined proceeding from coarse to fine refinement level and refining a cell whenever there exists a significant detail corresponding to this cell. For further details, we refer to Gerhard (2017).

It is important to emphasize that MRA operates on function spaces rather than discrete point values. Therefore, we represent the data as a function in the DG space. In our case, we use a *modal representation* of the DG function in our computations, i.e., each polynomial within a cell is described by its coefficients. This approach enables evaluation at arbitrary points within each cell by directly evaluating the corresponding polynomials, thus avoiding reconstruction. The application of the multiresolution-based grid adaptation and parameter choice will be discussed in detail in Sect. 3.

2.2.2 Data compression of ERA5 meteorological reanalysis data

In this section, we discuss the compression of ERA5 data using the multiresolution-based grid adaptation described in Sect. 2.2.1. Multiresolution-based grid adaptation can be extended to three dimensions. However, in this work, we perform grid coarsening of the three-dimensional fields by coarsening the two-dimensional slices for each pressure level separately. This approach helps to avoid scaling issues with variables that exhibit exponential variations with altitude. For simplicity, we focus on the compression of a single meteorological variable. Other meteorological variables are compressed in an analogous manner applying the compression to a vector field instead of a scalar field.

The starting point is a given two-dimensional field of discrete data $\tilde{u} := (u_{i,j})_{i=1,\ldots,N_x,j=1,\ldots,N_y}$ corresponding to the points $\tilde{x} := (x_{i,j})_{i=1,\ldots,N_x,j=1,\ldots,N_y}$. Here $N_x, N_y \in \mathbb{N}$ represent the number of points in longitudinal and latitudinal directions, respectively. To apply the multi-scale decomposition (4) to the data points $\tilde{u}$, it is necessary to interpret these data points as a function of the DG space (1) with order $p \in \mathbb{N}$. As described in Sect. 2.2.1, we define a sequence of nested grids $(\mathcal{G}_\ell)_{\ell=0,\dots,L}$ with maximum refinement level $L \in \mathbb{N}$. Note that the cells of the DG space grid do not necessarily coincide with those of the original grid for $\tilde{u}$. To project the values of $\tilde{u}$ onto the DG space, we perform a local projection on each cell $V_\lambda \in \mathcal{G}_\ell$. Since this projection involves integration over each cell, we employ Gauss-Legendre quadrature. For this purpose, it is necessary to evaluate data at quadrature points within every cell. In general, as these quadrature points do not coincide with the positions $\tilde{x}$ of the original data, we use a two-dimensional spline interpolation $S(\tilde{u})$ to interpolate between data points $\tilde{u}$. This spline interpolation allows us to compute intermediate values of $\tilde{u}$ using the polynomials consistent with those used in the DG space (1). Projecting the interpolated values $S(\tilde{u})$ yields the DG projection $u^\ell \in S_\ell$ on level $\ell \in \mathbb{N}$. For further details on this initial projection, see Algorithm 1.

Algorithm 1 Initial projection onto the DG space S_ℓ

```
Input: Discrete points values $\tilde{u} := (u_{i,j})_{i,j}$; order $p \in \mathbb{N}$ of the DG space; refinement level $L \in \mathbb{N}$;
Output: DG projection $u^L \in S_L$ on refinement level $L \in \mathbb{N}$
  $S(\tilde{u}) \leftarrow$ Spline interpolation of $\tilde{u}$
  for all $V_\lambda \in \mathcal{G}_L$ do
    $u^L_\lambda \leftarrow$ local DG projection using $S(\tilde{u})$ in cell $V_\lambda$
  end for
```

With the DG projection $u^L \in S_L$ of the original data, we can now perform multiresolution-based grid adaptation, as described in Algorithm 2. The main idea is to apply the multi-scale transformation on u^L to obtain the multi-scale decomposition (4) of u^L. After identifying the cells with significant details (5) we perform hard thresholding on the non-significant details to discard negligible contributions to the DG projection. This yields a sparse approximation (6). Finally, we perform the inverse multi-scale transformation to (6), resulting in a sparse approximation (10) in the DG space. For the sake of brevity, the details of the multi-scale transformation are omitted here. For further information, we refer to Gerhard et al. (2015), Gerhard and Müller (2016) and Gerhard (2017).

Algorithm 2 Data compression using multiresolution analysis

```
Input: DG projection $u^L$ on $S_L$; order $p \in \mathbb{N}$ of the DG space; refinement level $L \in \mathbb{N}$;
Output: Sparse approximation $u^{L,\varepsilon}$
    1. Perform local multi-scale transformation on $u^L$ to obtain the local multi-scale decomposition Equation (4).
    2. Perform hard-thresholding on the local detail coefficients $d^\ell_\lambda$ using (5) to obtain the sparse approximation (6) and the corresponding set of significant details $\mathcal{D}_{\ell,\varepsilon}$.
    3. Perform inverse local multi-scale transformation on (6) to obtain the sparse approximation (10) $u^{L,\varepsilon}$.
```

In the context of ERA5 meteorological reanalysis data, selecting an appropriate scaling C_{thresh} for the threshold value $\varepsilon_{\max}$ presents a significant challenge. Since the constant $C_{\text{thresh}} > 0$ in (11) acts as a filter, it must be set appropriately for each meteorological variable. The choice of C_{thresh} is crucial for ensuring the quality of the sparse approximation. If C_{thresh} is too large, important details may be lost; conversely, if chosen too small, the grid will be over-refined and the resulting compressed data will be too large. In this work, we present three possible strategies for selecting an appropriate value for the choice of C_{thresh} :

1. **Smallest amplitude:** In Gerhard and Müller (2016) and Gerhard (2017) an appropriate choice for C_{thresh} is discussed in the context of hyperbolic conservation laws. In these works, the authors select C_{thresh} as the smallest amplitude of the discontinuities.

2. **Pearson correlation coefficient:** The Pearson correlation coefficient is an important measure for describing the linear correlation between two datasets and thus indicates the quality of data compression, see Wegener (2013) and Tao et al. (2019). In Lemma 1 (see Appendix A) we show that a threshold value $\varepsilon_{\max} > 0$ can be determined such that a minimum correlation coefficient ρ_{min} between a DG function u^L and its sparse approximation $u^{L,\varepsilon}$ is achieved. By choosing
$$\varepsilon_{\max} \leq \frac{\text{Var}[u^L]\,(1-\rho_{\text{min}})}{C\,(1+\rho_{\text{min}})}$$
we can ensure $\rho(u^{L,\varepsilon}, u^L) \geq \rho_{\text{min}}$, where $\rho(u^L, u^{L,\varepsilon})$ is the Pearson correlation coefficient between two functions u^L and $u^{L,\varepsilon}$.

3. **Pressure level-dependent choice:** While it is feasible to select a thresholding value for a variable at a single pressure level, the data may vary significantly in magnitudes across different pressure levels. Therefore, applying a uniform chosen threshold parameter across all pressure levels is not appropriate. On the other hand, selecting individual threshold values for every variable and pressure level is impractical in practice. To address this issue, we determine a pressure level-dependent threshold value by taking the mean of all differences between neighbouring cells on the same pressure level:
$$\tilde{C}_{\text{thresh}} := C_{\text{user}} \cdot \frac{1}{|\mathcal{G}_L|} \sum_{\lambda \in \mathcal{G}_L} \frac{1}{|\mathcal{N}_\lambda|} \sum_{\mu \in \mathcal{N}_\lambda} \left| \bar{u}_\lambda^L - \bar{u}_\mu^L \right|. \tag{11}$$
Here, $\mathcal{N}_\lambda$ denotes all neighboring cells at level L of V_λ and $\bar{u}_\lambda^L$ is the mean value of the DG function in the cell $\lambda \in \mathcal{G}_L$.

Although Strategy 2 offers a mathematically rigorous choice for our thresholding procedure, its estimation tends to be overly conservative, leading to an overrefined grid and consequently low compression rates. Nonetheless, it establishes a solid framework for controlling the Pearson correlation coefficient in the context of multiresolution-based grid adaptation.

In this work, we utilize Strategy 3 which builds upon Strategy 1 while incorporating an appropriate choice of C_{thresh}. The approach described in (11) aims to automatically determine the smallest relevant amplitude, thereby accounting for variations in the magnitude of the data across pressure levels. Additionally, the user can fine-tune the coarsening process using the constant $C_{\text{user}} > 0$, which provides control over the quality of the compression.

After applying Algorithm 2 to the original data, the sparse representation $u^{L,\varepsilon}$ can be saved to a file, where all DG coefficients are stored along with their corresponding cell identifier $\lambda \in \mathcal{I}_{L,\varepsilon}$. Each cell is identified by its *levelmultiindex*, denoted as `(level, {mi_1, mi_2})`. A levelmultiindex specifies both the refinement level of the cell and its absolute position on the Cartesian grid at the level. Consequently, the DG function is represented as a mapping from a set of levelmultiindices to their associated DG coefficients.

Given the maximum refinement level, the order of the DG space, the number of cells on the coarsest grid and the domain of the data, storing each DG coefficient with its cell information is sufficient to reconstruct all data. To efficiently store a levelmultiindex, we encode it as a single variable of 8 byte unsigned integer. Specifically, the refinement level is encoded using 4 bits and each directional index (`mi_1` and `mi_2`) uses 20 bits. This encoding allows representation of grids with up to 16 refinement levels and up to 1 048 576 cells per direction, which is more than sufficient for our purposes. Additionally we store $|\mathcal{P}|$ coefficients for each cell. Applying a lossless compression algorithm such as ZSTD (https://github.com/facebook/zstd) further increases the overall data compression. Algorithm 3 outlines the overall procedure of the data compression routine using multiresolution analysis.

Algorithm 3 Data compression using multiresolution-based grid adaptation

```
Input: Two dimensional data field $\tilde{u}$; order of the DG space $p$; maximum refinement level $L$; threshold value $C_{\text{user}}$
Output: Compressed data file
    1. Initialize basis functions for single-scale and multi-scale spaces
    2. $u^L \leftarrow \tilde{u}$ Project initial point data of $\tilde{u}$ using spline interpolation (Algorithm 1)
    3. Determine $C_{\text{thresh}}$ using (11)
    4. $u^{L,\varepsilon} \leftarrow$ sparse approximation using hard thresholding (Algorithm 2)
    5. Store adaptive grid and the corresponding DG coefficients in a file
```

Data compression with multiresolution-based grid adaptation provides an easy-to-use method that allows users to control the quality of the compression with adjusting only a few parameters. Moreover, this approach enables direct control over the perturbation error (8). A comprehensive evaluation of the effects of different parameters choices will be discussed in Sect. 3. In the following section, we introduce a module that implements all algorithms required for performing multi-scale based grid adaptation.

2.2.3 Data compression using MRA-MW

Data compression is performed using the MRA-MW library (https://git-ce.rwth-aachen.de/igpm/mra-mw) which is derived from the first-order hyperbolic partial differential equation solver *MultiWave* (https://www.igpm.rwth-aachen.de/forschung/multiwave). The primary objective of the MRA-MW library is to provide an easy-to-use `C`-interface to MultiWave's grid adaptation module.

To ensure a simple interface, the required data structures are abstracted through the `mra_mw_module_t` struct. This struct handles the creation of all internal data structures and manages the construction of necessary basis functions. This setup can be completed prior to any simulation and reused for different variables on the same initial grid. The DG function itself is represented by the `mra_mw_sol_t` struct, which contains the DG data – a vector of hash maps – describing the stored DG coefficients along with their corresponding cells. All user-defined parameters are collected in the `mra_mw_parameter_t` struct. As hash maps we use the *unordered_dense* library (https://github.com/martinus/unordered_dense). These parameters include properties of the original data, such as the number of points in the x-direction (`nx`) and y-direction (`ny`), the spatial `domain`, the number of cells on the coarsest grid for the DG approximation (`Nd0_x`, `Nd0_y`), the maximum refinement level (`max_level`) and the grid parameters `Nd0_x` and `Nd0_y`. Note that many parameters can be reused for the compression of ERA5 data and only need to be set once. When compressing a single two-dimensional field, the user typically only needs to specify the thresholding parameter `C_thresh` and the maximum refinement level `max_level`. The order p of the DG space is set via the preprocessor variable `PDIM` due to changes in internal data structures.

An example of the usage of MRA-MW for compressing a two-dimensional field is shown in Alg. 4. The MRA-MW implementation closely follows Algorithm 3 while minimizing additional technical overhead wherever possible. For the spline interpolation we use the spline module of the GNU Scientific Library (GSL, https://www.gnu.org/software/gsl/). In addition to `mra_mw_save_sol`, there is also a function `mra_mw_read_sol`, which reads both the DG data and its associated multi-scale object. The function `mra_mw_eval` allows evaluations at arbitrary data points $x \in \mathbb{R}^2$ within the DG function, making access to data straightforward for users. An example demonstrating how MRA-MW is integrated into MPTRAC will be presented in Sect. 2.2.5.

2.2.4 MPTRAC

The Massive-Parallel Trajectory Calculation (MPTRAC) Lagrangian transport model has been under development since 2013, with its main purpose being the calculation of air parcel trajectories (Hoffmann et al., 2016, 2022, 2025). MPTRAC has been applied since its first release for several case studies; primarily studies focusing on the transport of SO_2 from volcanic eruptions (e.g. Liu et al. (2023) and references therein). The air parcel trajectories are calculated using 4-D linear interpolation of given wind fields and the explicit midpoint method for numerical integration of the kinematic equations of motion (Rößler et al., 2018). The quality of the air parcel trajectories was evaluated by comparison to super-pressure balloon observations for the Antarctic lower stratosphere (Hoffmann et al., 2017). In the following we focus the description on the MPTRAC modules that have been used in this study. A detailed description of the model can be found in Hoffmann et al. (2016, 2022).

MPTRAC consists of several modules that allow to calculate additional processes either along the trajectories or separately. One of the modules that can be used separately is the module `met_conv` which can be used for the conversion/compression of meteorological reanalysis data files. Using `met_conv` data stored in the NetCDF format can be compressed with the following conventional compressors: Zstandard (ZSTD, https://github.com/facebook/zstd), ZFP (https://computing.llnl.gov/projects/zfp) and layer packing (PCK, Silver and Zender, 2017). The usage and application of these within MPTRAC is described in Khosrawi and Hoffmann (2025). Newly added to MPTRAC and what has been used in this study is compressing

Algorithm 4 MRA-MW example for using the data compression Algorithm 3 for a two-dimensional data field.

```
// Initialize multi-scale object
mra_mw_param_t* param_ptr = mra_mw_set_parameters(nx, ny, max_level, Nd0_x, Nd0_y, domain);
mra_mw_module_t* multiscale_ptr = mra_mw_init(param_ptr);

// Algorithm 1: Create DG projection on max_level using spline interpolation
mra_mw_solution_t* solution_ptr = mra_mw_read_arr(multiscale_ptr, data_array, x, y);

// Set thresholding parameter as in Equations (7), (11)
mra_mw_set_eps(multiscale_ptr, solution_ptr, C_thresh);

// Algorithm 2: Data compression using MRA
mra_mw_coarsening(multiscale_ptr, solution_ptr);

// Saving sparse DG representation to a file
mra_mw_save_sol(solution_ptr, output_file);

// Point evaluation of the DG-representation for a given point x
double x[2];
double u[1];
mra_mw_eval(multiscale_ptr, solution_ptr, x, u);

// Cleaning
mra_mw_delete_sol(solution_ptr);
mra_mw_delete_module(multiscale_ptr);
mra_mw_delete_param(param_ptr);

```

the data using MRA-MW, thus using grid adaptation to compress the meteorological data (see Sect. 2.2.1). The NetCDF files are compressed using the respective compression libraries that have been coupled to MPTRAC. The new data are then written out in a binary C format using the respective name of the compression method as file name suffix. These binary C files can then be read again with MPTRAC either to convert these back to NetCDF (decompression) for further analysis or using them for trajectory calculations.

The MPTRAC module `traj` has been used for the trajectory calculations. Using this module, the pure advection of an air parcel is calculated. We simulated 10-day forward trajectories starting on 1 January 2017 for 10^4 air parcels that have been globally distributed over the altitude range of 2–48 km. Application of the module `atm_dist` allows to calculate the statistics between deviations of two sets of trajectories. Here, this refers to the deviations between the trajectories calculated using the original ERA5 NetCDF files and the ones calculated using the compressed reanalysis files as input.

2.2.5 Coupling of MPTRAC with MRA-MW

To integrate MRA-MW in MPTRAC, we enhanced the build system of MRA-MW enabling its compilation as an external library. Additionally, we developed a C wrapper to facilitate direct linking of MRA-MW with MPTRAC. To further enhance usability, we designed a simple and user-friendly application interface for MRA-MW.

The function `mra_mw_set_parameters()` is used to define method parameters, while `mra_mw_init()` initializes MRA-MW. For ingesting 2-D or 3-D array data on a regular Cartesian grid, the function `mra_mw_read_arr()` has been made available. Adaptive mesh refinement and data compression are handled by `mra_mw_coarsening()`. Users can set the global threshold value ε_{max} individually for each meteorological variable using `mra_mw_set_eps()`. The function `mra_mw_compression_rate()` allows users to calculate the compression ratio achieved through grid adaptation. To perform polynomial evaluations on adaptive grid data at specific locations, the function `mra_mw_eval()` is provided. For managing adaptive grid data, `mra_mw_read_sol()` and `mra_mw_save_sol()` handle reading and writing the data to disk. Finally, `mra_mw_delete_sol()` and `mra_mw_delete_module()` are used to finalize operations with MRA-MW and release temporary memory.

Using the MRA-MW application interface described here, the new function `compress_mra_mw()` in MPTRAC provides the mechanism for compressing and decompressing multi-scale grid data in Cartesian coordinates. It first configures the MRA-MW parameters, including the resolution, domain, and maximum refinement levels. For decompression, the function reads the compressed data stream from disk, reconstructs the adaptive grid, and evaluates the data at original Cartesian grid points, storing the results in a 3-D array. During compression, it processes the input array in batches, performs adaptive mesh refinement using user-specified threshold values, and outputs the compressed data stream. The function also evaluates key metrics such as compression ratio and the accuracy of the compressed representation. The function concludes by releasing all allocated resources, ensuring proper memory management. The function `compress_mra_mw()` enables seamless integration of meteorological data compression and decompression with MRA-MW in MPTRAC. It works in a similar manner compared to other compression methods for meteorological data already implemented in MPTRAC. Note that the MRA-MW library is thread-safe, enabling the use of shared memory parallelization, such as OpenMP, to simultaneously compress multiple data on different pressure levels.

2.3 Evaluation metrics

2.3.1 Efficiency metrics

The efficiency in data reduction that is achieved due to the compression with the adaptive grids is assessed by using the compression ratio (CR). The CR is defined as the quotient of the size of the original data file (F_{orig}) divided by the size of the compressed data file (F_{compr}),

$$\mathrm{CR}(F) = \frac{\mathrm{filesize}(F_{\text{orig}})}{\mathrm{filesize}(F_{\text{compr}})}. \tag{12}$$

2.3.2 Statistical metrics

To evaluate the accuracy of the reanalysis data after compression with MRA-MW we use the following statistical metrics: root mean square error (RMSE), normalised root mean square error (NRMSE), the relative ℓ^∞ error (e_∞) and Pearson correlation coefficient (r_{xy}).

The root mean square error is calculated by:

$$\mathrm{RMSE} = \sqrt{\frac{1}{N}\sum_{i=1}^{N}(|x_i - y_i|)^2} \tag{13}$$

where $x_i - y_i$ is the absolute difference between each data point x_i and y_i of the data sets x and y, which are in our case the compressed and reference data, respectively.

In addition to the RMSE, the normalised RMSE (NRMSE) is considered, which is defined as follows:

$$\mathrm{NRMSE} = \frac{\mathrm{RMSE}}{R_y} \tag{14}$$

where R_y is the range of y, thus the difference of the maximum and minimum value of the reference data $R_y = y_{\text{max}} - y_{\text{min}}$.

The Pearson correlation coefficient is defined as:

$$r_{xy} = \frac{\sum_{i=1}^{N}(x_i - \bar{x})(y_i - \bar{y})}{\sqrt{\sum_{i=1}^{N}(x_i - \bar{x})^2 \sum_{i=1}^{N}(y_i - \bar{y})^2}} \tag{15}$$

where N is the sample size, x_i and $\bar{x}$ are the values and mean of the compressed data and y_i and $\bar{y}$ are the values and mean of the original data. In previous studies of Wegener (2013) and Tao et al. (2019) it was suggested that the correlation coefficient between original and reconstructed data should be at least $r_{\text{min}} > 0.99999$ (“five nines”) or better for a minimal loss due to compression. We use this value as guidance.

Finally, we define the relative ℓ^∞–error as follows:

$$e_\infty = \frac{|\boldsymbol{x} - \boldsymbol{y}|_{\ell^\infty}}{|\boldsymbol{y}|_{\ell^\infty}} = \frac{\max_{i=1,\dots,N}|x_i - y_i|}{\max_{i=1,\dots,N}|y_i|}, \tag{16}$$

where $\boldsymbol{x} = (x_i)_{i=1,\dots,N}$ represents the data points of the compressed data and $\boldsymbol{y} = (y_i)_{i=1,\dots,N}$ denotes the data points of the original data.

2.3.3 Trajectory metrics

The accuracy of the trajectory calculation is assessed by considering the spatial differences between two sets of trajectories (here the trajectories that are calculated based on the compressed and uncompressed reanalysis data files, respectively). The absolute horizontal (AHTD) and vertical transport deviation (AVTD) can be calculated as follows (Kuo et al., 1985; Rolph and Draxler, 1990; Stohl, 1998):

$$\mathrm{AHTD}(t) = \frac{1}{N}\sum_{i=1}^{N}\sqrt{[X_i(t)-x_i(t)]^2+[Y_i(t)-y_i(t)]^2} \tag{17}$$

$$\mathrm{AVTD}(t) = \frac{1}{N}\sum_{i=1}^{N}|Z_i(t)-z_i(t)| \tag{18}$$

where $X_i(t)$, $Y_i(t)$ and $Z_i(t)$ as well as $x_i(t)$, $y_i(t)$ and $z_i(t)$ refer to the particle coordinates of the two sets of trajectories. The relative horizontal transport deviations (RHTDs) and relative vertical transport deviations (RVTDs) can then be calculated by dividing the absolute transport deviations by the horizontal or vertical path lengths of the trajectories, respectively (Rößler et al., 2018; Hoffmann et al., 2019, 2022).

3 Results

3.1 Illustration of multiresolution-based grid adaptation

Before we start with the investigation of data compression, we would like to demonstrate how our approach impacts the data. Starting from the original regular-sized $0.3° \times 0.3°$ grid of the ERA5 data, Fig. 1 illustrates the global water vapor field at standard pressure (1013.25 hPa). For grid points where the surface pressure is lower than the standard pressure, the values at 1013.25 hPa are obtained by extrapolation from the surface level. In this example, an order of `PDIM` $= 3$ has been used for the discontinuous Galerkin (DG) space. The initial grid at the coarsest refinement level consists of `Nd0_x` $= 6$ in the x-direction and `Nd0_y` $= 3$ cells in the y-direction, with a maximum refinement level `max_level` $= 8$.

We first transform the point-based values into the DG space, as shown in Algorithm 1. Then we apply multiresolution-based grid adaptation to compress the data, as detailed in Algorithm 3. This process removes cells in areas where no significant information is present while maintaining the original resolution in regions where significant variability is detected as, e.g. in filamentary structures in the water vapour field. In addition to the global water vapour field shown in Fig. 1, two zoomed-in regions are provided to better visualize how the grid is adapted. Here, an area with a filament (tongue-like structure) has been selected. In examining the second zoomed-in figure, one can clearly see the fine grid within the filament area and a coarser grid in areas outside of the filament. We would like to emphasize that the data in each cell is presented as a polynomial and does not need to be constant.

By adjusting the threshold values C_{thresh}, the order of the DG space p and the values `Nd0_x` and `Nd0_y` the grid can be adapted and the data can be compressed according to the needs of the user concerning the size and accuracy of the compressed files. In the following we describe how the thresholding values C_{thresh} have been optimized and the compression tests we have performed with adjusting the order of the DG space `PDIM`, the maximum level of refinement `max_level` and `Nd0_x` and `Nd0_y`.

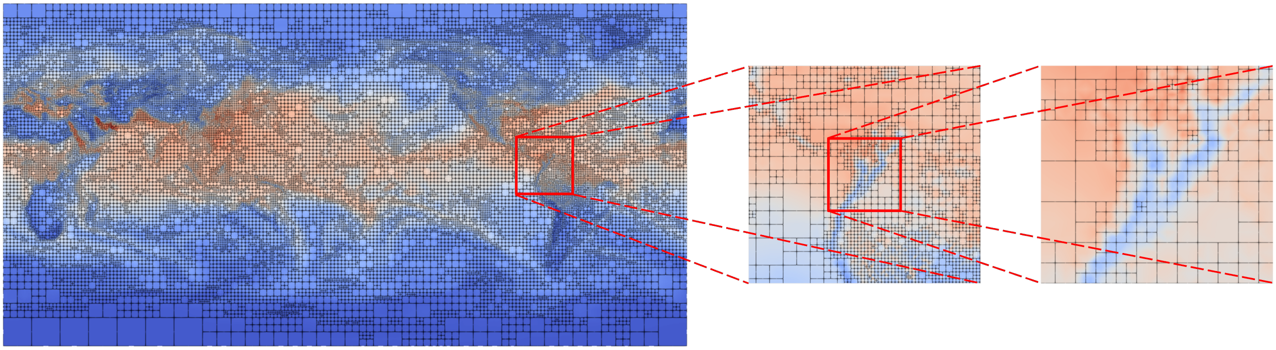

Figure 1. Compressed ERA5 water vapor field at 1013.25 hPa on 1 January 2017, 00:00 UTC, using multiresolution-based grid adaptation with order `PDIM` = 3, maximum refinement level `max_level` = 8, `Nd0_x` = 6 and `Nd0_y` = 3.

3.2 Optimizing the thresholding value C_{thresh}

As a first step we used MRA-MW alone to adjust the C_{thresh} values for each meteorological parameter to be compressed so that we derive the highest possible correlation coefficients to be as lossless as possible. We then repeated the same procedure with MRA-MW coupled to MPTRAC to optimize these values and to take also into account the resulting efficiency in compression. From the ERA5 data files all 3-D fields are compressed. These are the fields of the following meteorological parameters: geopotential height (GPH), temperature (T), zonal wind (u), meridional wind (v), vertical velocity (ω), potential vorticity (PV), water vapour (H_2O), ozone (O_3), liquid water content (LWC), rain water content (RWC), ice water content (IWC), snow water content (SWC) and cloud water content (CC).

The optimized C_{thresh} values for each meteorological parameter to be compressed have been set in `mptrac.c` as default values and can be changed by the user using the respective control parameters. The current optimized values $C_{\text{thresh,opt}}$ are as follows: For T, u and v these have been set to 0.05 and for all other parameters to 1.0. If for example, for temperature the threshold value C_{thresh} is supposed to be changed from 0.05 to 0.01 this is done by using the control parameter `MET_MRA_MW_EPS_T` and adding in the run script additional to calling `met_conv` the control parameter and the respective value `MET_MRA_MW_EPS_T 0.01`.

Figure 2 shows the compressed temperature field from ERA5 at 10 km compressed by using a C_{thresh} value of 0.2 and 0.05, respectively, and an order of the DG space of `PDIM` = 2 and `PDIM` = 3, respectively. Decreasing C_{thresh} from 0.2 to 0.05 leads to a finer adaptive grid, while a higher order of the DG space results in a coarser grid and thus higher compression.

3.3 Efficiency of compression

To assess the efficiency of the compression with the multiresolution-based grid adaptation we performed six compression tests where we used a maximum level of refinement `max_level` of 6, 7 and 8 and an order of the DG space of `PDIM` = 2 and 3. In Table 1 the compression ratios, file size and time required to compress one file of ERA5 data for these test cases are summarised. In these compression tests `Nd0_x` = 6 and `Nd0_y` = 3 are used. The tests are named using a four digit number

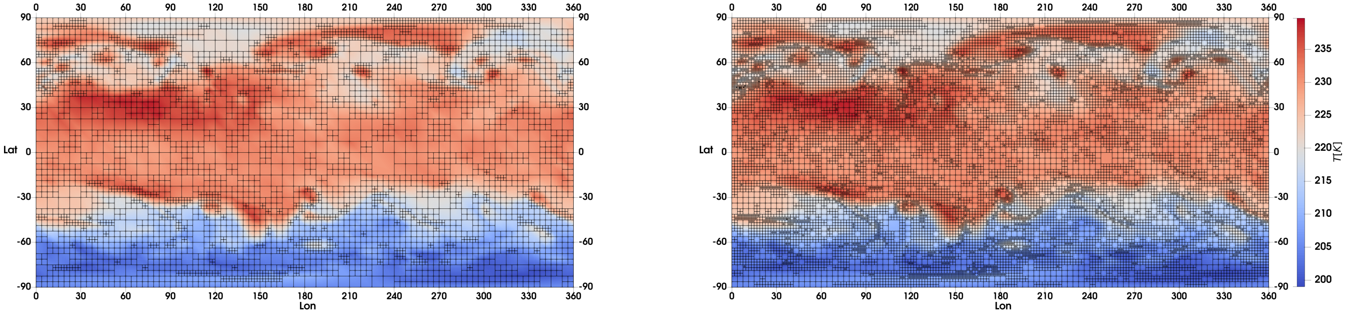

(a) $\texttt{PDIM} = 2,\ C_{\text{thresh}} = 0.2$ (b) $\texttt{PDIM} = 2,\ C_{\text{thresh}} = 0.05$

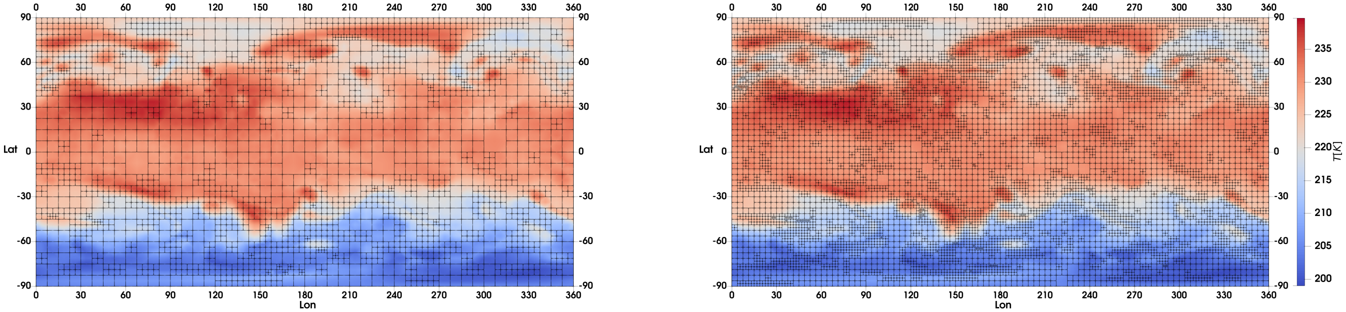

(c) $\texttt{PDIM} = 3,\ C_{\text{thresh}} = 0.2$ (d) $\texttt{PDIM} = 3,\ C_{\text{thresh}} = 0.05$

Figure 2. Compressed ERA5 temperature field on 1 January 2017, 00:00 UTC, using multiresolution-based grid adaptation with various orders `PDIM` and scalings C_{thresh} for the threshold value .

which consists of the order of the DG space, the maximum level of refinement and the used `Nd0_x` and `Nd0_y` values. For example, 2663 means that the order of the DG space is $\texttt{PDIM} = 2$, the maximum level of refinement of $\texttt{max\_level} = 6$ and $\texttt{Nd0\_x} = 6$ and $\texttt{Nd0\_y} = 3$ is used.

The highest compression is achieved for the compression tests MRA_MW_2663 and MRA_MW_3663 (CR of 12.6 and 11.0, respectively). The file size is reduced from 4.9 GB to 400 MB and 465 MB, respectively. The lowest compression is derived for the compression tests MRA_MW_2863 and MRA_MW_3863 (CR of 1.6 and 1.9, respectively). Here, the file sizes are reduced from 4.9 GB to 3.1 GB and 2.6 GB. The compression tests MRA_MW_2763 and MRA_MW_3763 are in between and have a compression ratio of 4.5 and the file size is reduced to 1.1 GB in both cases. These compression tests show that depending on the set-up used, compression ratios ranging from 1.6 to 12.6 are yielded (Table 1). The question now is, how lossy are the compressed data and how can the best compromise between compression ratio and accuracy be found? This will be evaluated and discussed in the next section.

Table 1. Summary of the results of the compression tests performed (file size, compression ratio (CR) and time to compress), using different orders of the DG space p (`PDIM`) and maximum level of refinement L (`max_level`). The first number in the test case name refers to the order of the DG space, the second gives the maximum level of refinement and the last two to the chosen `Nd0_x` and `Nd0_y` values. Compression times in the table refer to compression times required on the JUWELS Cluster supercomputer at the Jülich Supercomputing Centre, using a single compute node consisting of two Intel Xeon Platinum 8168 CPUs with 2×24 cores.

Test no.	Test name	File size	CR	Time
1	MRA_MW_2663	400 MB	12.6	23 s
2	MRA_MW_2763	1.1 GB	4.5	59 s
3	MRA_MW_2863	3.1 GB	1.6	198 s
4	MRA_MW_3663	465 MB	11.0	31 s
5	MRA_MW_3763	1.1 GB	4.5	82 s
6	MRA_MW_3863	2.6 GB	1.9	257 s

Table 2. Correlation coefficient r_{xy} at $10\,\mathrm{km}$ for each meteorological parameter for the six compression tests that have been performed using different orders of the DG space and level of refinement (see Table 1).

Parameter	MRA_MW_2663	MRA_MW_2763	MRA_MW_2863	MRA_MW_3663	MRA_MW_3763	MRA_MW_3863
GPH	0.99990	0.99998	0.99999	0.99995	0.99999	0.99999
U	0.99821	0.99964	0.99994	0.99874	0.99976	0.99996
V	0.99756	0.99948	0.99991	0.99813	0.99966	0.99995
ω	0.98767	0.99460	0.99916	0.98783	0.99766	0.99963
T	0.99789	0.99949	0.99990	0.99859	0.99964	0.99993
H_2O	0.99866	0.99982	0.99997	0.99963	0.99992	0.99999
O_3	0.99961	0.99993	0.99999	0.99979	0.99996	0.99999

3.4 Accuracy of compression

In the studies by Wegener (2013) and Tao et al. (2019) a correlation coefficient of at least $r_{\text{min}} = 0.99999$ was suggested in order to achieve a minimal loss when compressing the data. We use this value as reference and try to get as close as possible. In Table 2 the correlation coefficients for the six compression tests described in the previous section are summarised. For some of the parameters a correlation coefficient $r_{xy} \geq r_{\text{min}}$ is achieved. Thereby, the highest correlation coefficients are derived for the compression test MRA_MW_3863 and the lowest correlation coefficients are derived for the compression test MRA_MW_2663. Thus, this shows that generally, as expected, the stronger the compression, the greater the loss of accuracy. However, for the test case MRA_MW_3863 a higher compression rate than for MRA_MW_2863 is derived with additionally maintaining a higher accuracy.

For test cases MRA_MW_2763 and MRA_MW_3763 the same file size and compression rate is derived, but the correlation coefficients are higher for MRA_MW_3763. If we additionally take the time required for compression into account (Table 1), we see that for achieving a higher accuracy we need more time. From these six test cases, the test case MRA_MW_3763 seems to be a good compromise in terms of compression speed, file size/compression ratio and accuracy.

For the compression tests discussed above we kept the values for `Nd0_x` $= 6$ and `Nd0_y` $= 3$ fixed. We performed additional tests with changing these values (Table 3). Taking the test cases MRA_MW_2763 and MRA_MW_3763 as reference we assess what happens when `Nd0_x` is set to a value of 8 and `Nd0_y` to a value of 4. Increasing `Nd0_x` and `Nd0_y` results for both test cases (MRA_MW_2784 and MRA_MW_3784) in higher correlation coefficients for all parameters except ω (Table 4), but the compression ratio is slightly lower. Thus, increasing `Nd0_x` and `Nd0_y` is useful when a higher accuracy is desired. On the other hand if already a high accuracy of the compressed data is reached, `Nd0_x` and `Nd0_y` can be decreased, setting these to 4 and 2, respectively. If we take the test cases where we derived the highest correlation coefficients, MRA_MW_2863 and MRA_MW_3863, as reference (Table 1) and compare these to the additional compression tests MRA_MW_2842 and MRA_MW_3842 (Table 4) we find that the correlation coefficients are slightly lower, but that a higher compression is derived.

Table 3. Summary of the results of the compression tests performed (file size, compression ratio (CR) and time to compress), using different `Nd0_x` and `Nd0_y`. The same notation for the test cases as in Table 1 is used. Compression times in the table were required on the JUWELS Cluster supercomputer at Jülich Supercomputing Centre using a single compute node consisting of two Intel Xeon Platinum 8168 CPUs with 2×24 cores.

Test no.	Test name	File size	CR	time
7	MRA_MW_2784	1.7 GB	2.9	91 s
8	MRA_MW_2842	1.7 GB	2.9	86 s
9	MRA_MW_3784	1.6 GB	3.1	128 s
10	MRA_MW_3842	1.6 GB	3.1	126 s

Comparing MRA_MW_2784 with MRA_MW_2842 and MRA_MW_3784 with MRA_MW_3842, respectively, we find that these set-ups lead to the exact same results concerning compression rate and correlation coefficient, only the time required for compression is with using `Nd0_x` $= 4$ and `Nd0_y` $= 2$ slightly faster. Figure 3 shows the compression ratio and file size for each test case. This figure summarizes the results of the 10 compression tests. Clearly visible is here that with `PDIM` $= 2$ higher compression ratios can be achieved for stronger compression cases. For the weaker compression cases it is the opposite (see also Table 1 and Table 3), here stronger compression is achieved with `PDIM` $= 3$.

From the above tests we found that when decreasing `Nd0_x` and `Nd0_y` to 4 and 2 instead of 6 and 3, the correlation of e.g. T and ω degraded significantly. Therefore, as a last compression test we changed C_{thresh} for T and ω from 0.05 to 0.01 for T and from 0.05 to 0.1 for ω, respectively using the compression tests MRA_MW_2842 and MRA_MW_3842 as reference (not shown in the table and figures since this changes only two values). For MRA_MW_2842 the correlation coefficient of T improved from 0.99973 to 0.99996 and for ω from 0.99751 to 0.99908. For MRA_MW_3842 the improvement of the

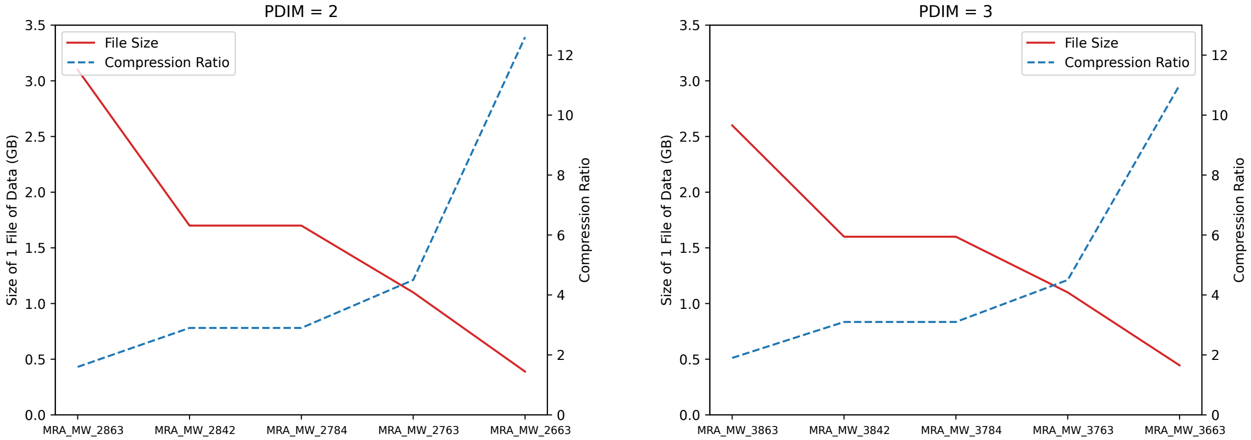

Figure 3. Compression ratio and file size for the compression tests using `PDIM` = 2 (left) and `PDIM` = 3 (right).

correlation coefficient is not as high since here the correlation coefficients are already high, but still significant. The correlation coefficient of T is improved from 0.99982 to 0.99998 and for ω from 0.99893 to 0.99994. The file sizes increase from 1.7 to 2.7 GB for MRA_MW_2842 and from 1.6 to 2.8 GB resulting in a compression ratio of 1.8 for both.

Figure 4 shows the correlation coefficient for the 10 test cases that were listed in Table 1 and Table 3 sorted based on the increasing correlation of the test cases. For better visibility the parameter ω is shown in a separate panel. This figure clearly shows that for the test cases MRA_MW_2663, MRA_MW_3663 and MRA_MW_2763 the loss due to compression is quite strong and that here the correlation coefficients are far below the desired correlation r_{min}. For the compression tests CM_3763, MRA_MW_2842, MRA_MW_2784, MRA_MW_3784 the correlations are increasing and have an intermediate loss in accuracy, while for MRA_MW_2863 and MRA_MW_3863 the highest correlation coefficients are derived that are also closest to the desired correlation r_{min}.

Table 4. Correlation coefficient r_{xy} at 10 km for each meteorological parameter for the additional compression tests using different `Nd0_x` and `Nd0_y`.

Parameter	MRA_MW_2784	MRA_MW_2842	MRA_MW_3784	MRA_MW_3842
GPH	0.99999	0.99999	0.99999	0.99999
U	0.99983	0.99983	0.99989	0.99989
V	0.99975	0.99975	0.99985	0.99985
ω	0.99751	0.99751	0.99893	0.99893
T	0.99973	0.99973	0.99982	0.99982
H_2O	0.99992	0.99992	0.99996	0.99996
O_3	0.99997	0.99997	0.99998	0.99998

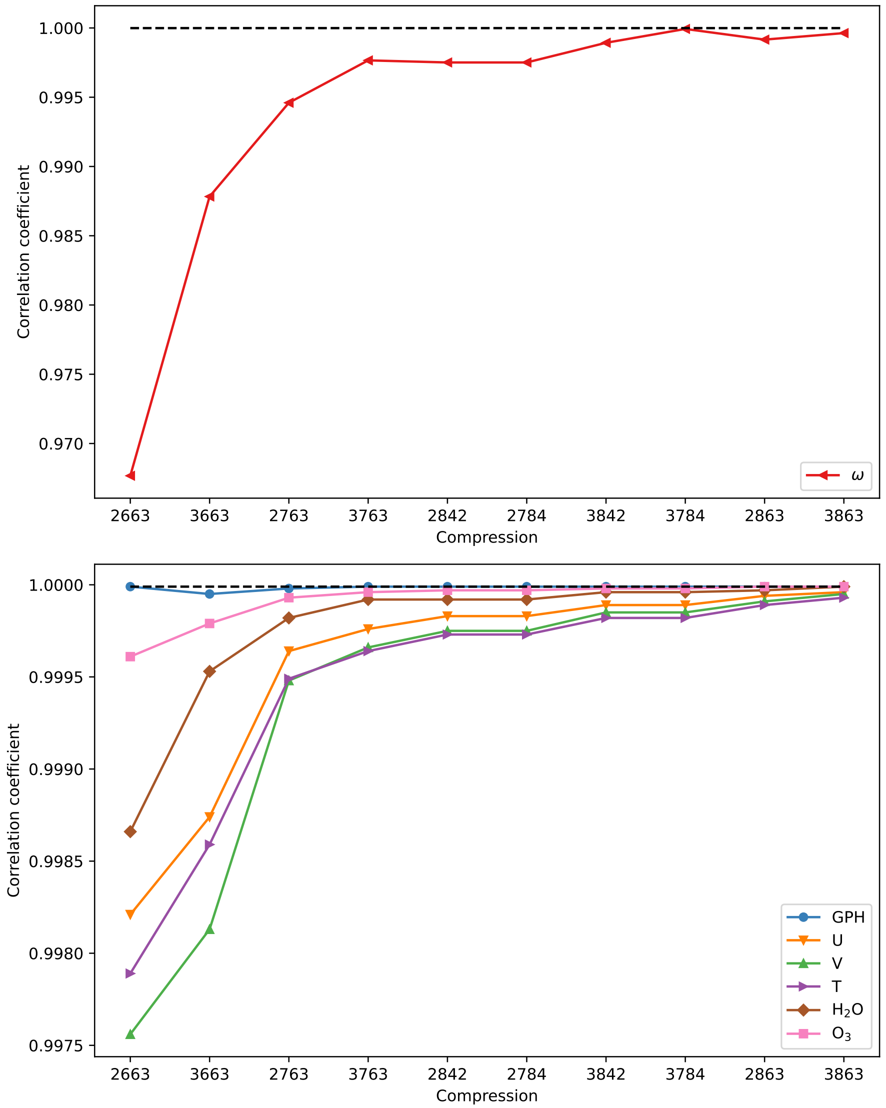

Figure 4. Correlation coefficients for the compression tests listed in Table 1 and 3 using different orders of the DG space `PDIM`, maximum level of refinement `max_level` and `Nd0_x`, `Nd0_y` for vertical wind (ω) (top) and for all other parameters (bottom).

A similar behaviour is found for the NRMSE (Fig. 5). Stronger compression leads to higher NRMSE values. The lowest NRMSEs are here also found for the compression experiments MRA_MW_2863 and MRA_MW_3863. This means in order to achieve a near-lossless accuracy we currently can only compress the ERA5 data with a compression ratio of 1.6 or 1.9, respectively.

To investigate the effect of C_{thresh} on the compressed ERA5 data, we compare both the relative ℓ^{∞}–error as well the correlation coefficient between the compressed data and the original data for increasing threshold values in Fig. 6 and Fig. 7,

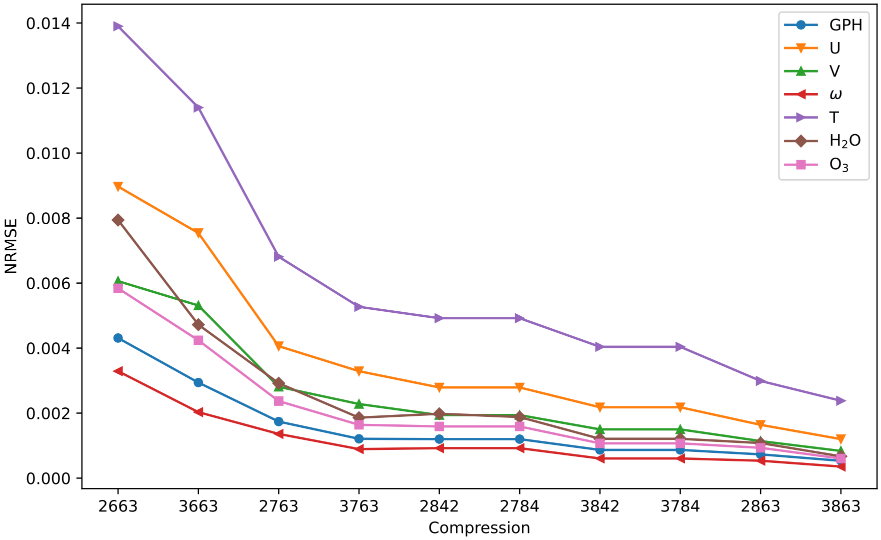

Figure 5. NRMSE for the compression tests using different orders `PDIM` of the DG space, maximum refinement levels `max_level` and `Nd0_x` and `Nd0_y`.

respectively. As a baseline, we use the optimized values $C_{\text{thresh, opt}}$ suggested in Sect. 3.2 and multiply them by a factor of 2^N for $N = 1, \ldots, 5$, i.e., $C_{\text{thresh}} = 2^N \times C_{\text{thresh, opt}}$. As the threshold value increases, the original data are represented on a coarser grid with fewer cells, which leads to higher compression ratios. Consequently, the quality of the compressed data is expected to deteriorate for larger threshold values. In the following, we fix the configuration to `MRA_MW_3863`.

In Fig. 6, we show the effect of different threshold values on the relative ℓ^∞–error. For each variable, we show the mean relative ℓ^∞–error over all pressure levels as well as the maximum relative ℓ^∞–error over all pressure levels. We observe that the default values provided in Sect. 3.2 lead to very small relative ℓ^∞–errors for all variables. As C_{thresh} increases and thus the compression of the data, the relative error increases for all variables. We also observe that the maximum relative error over all pressure levels is significantly larger than the mean error. These larger errors occur on pressure levels with highly heterogeneous data as can be concluded from plots not presented here.

In Fig. 7, we show the influence of the different threshold values on the correlation coefficient and the minimum correlation coefficient over all pressure levels. We observe a similar behaviour to that of the relative ℓ^∞–error: as the threshold value increases, the correlation coefficient decreases. In contrast to the relative error, however, the correlation coefficient appears to be more sensitive to changes in C_{thresh}. This can be explained by outliers in the compressed data when it is projected onto a coarser grid, which have a significant impact on the correlation coefficient. Overall, we conclude that an appropriate choice of the scaling factor for the threshold value C_{thresh} is crucial for the quality of the compression.

In order to derive a higher compression rate with at the same time maintaining a high accuracy, we combine our multiresolution-based compression with the lossless compressor ZSTD.

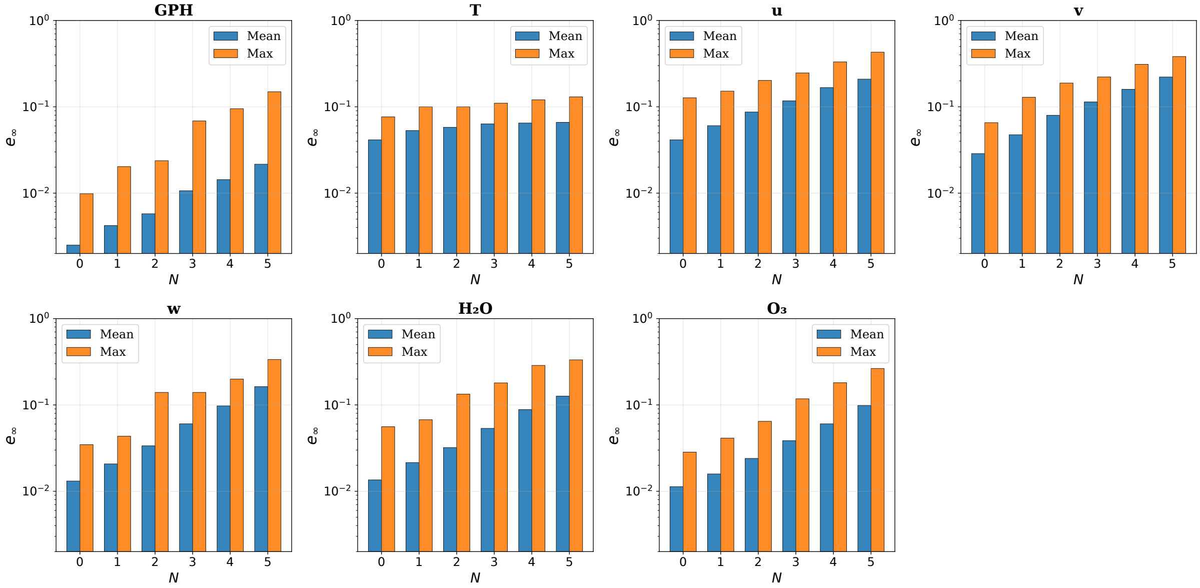

Figure 6. Relative ℓ^∞–error using different threshold values $C_{\text{thresh}} = 2^N \times C_{\text{thresh, opt}}$.

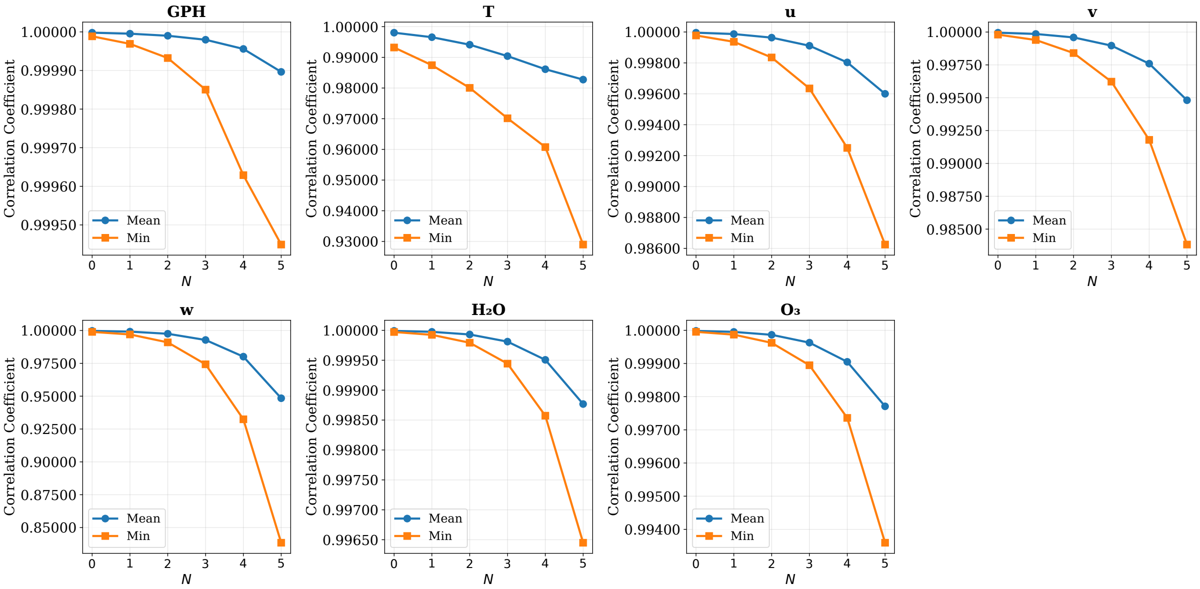

Figure 7. Correlation coefficient using different scalings of the threshold value $C_{\text{thresh}} = 2^N \times C_{\text{thresh, opt}}$.

3.5 Additional compression with ZSTD

In previous studies it has been shown that by combining different compression algorithms, lossy methods followed by lossless methods in particular, compressors can achieve higher compression ratios (e.g. Delaunay et al., 2019; Klöwer et al., 2021; Böing et al., 2024). Here we added ZSTD on the MRA-MW data streams, a lossless compression method, to increase the compression of the ERA5 data.

In the MPTRAC version used here (v2.7), `mra_mw_sol` had to be replaced in the code (`mptrac.c`) by `mra_mw_sol_zstd` to enable additional ZSTD compression. In MPTRAC v2.8 a new control parameter has been added that enables the additional compression with ZSTD. For this the control parameter MET_MRA_MW_ZSTD should be set to "1" for additional ZSTD compression and to "0" for no additional ZSTD compression (`MET_MRA_MW_ZSTD=1` and `MET_MRA_MW_ZSTD=0`, respectively).

Compared to the compression results in Table 1 and Table 3, we observe that applying an additional lossless compression stage to the already compressed data further reduces the file size of up to 30%, however at the cost of increased computational time (Table 5).

Table 5. Same compression tests as for Table 1 and Table 3, but with additional ZSTD compression. The first number in the test case name refers to the order of the DG space, the second gives the maximum level of refinement and the last two to the chosen `Nd0_x` and `Nd0_y` values. Compression times in the table were required on the JUWELS supercomputer (see Table 1 and Table 3)

Test no.	Test name	File size	CR	time
1	MRA_MW_2663	299 MB	16.4	40 s
2	MRA_MW_2763	793 MB	6.2	117 s
3	MRA_MW_2863	2.2 GB	2.2	370 s
4	MRA_MW_3663	384 MB	12.7	55 s
5	MRA_MW_3763	933 MB	5.3	142 s
6	MRA_MW_3863	2.2 GB	2.2	424 s
7	MRA_MW_2784	1.2 GB	4.1	184 s
8	MRA_MW_2842	1.2 GB	4.1	169 s
9	MRA_MW_3784	1.4 GB	3.5	214 s
10	MRA_MW_3842	1.4 GB	3.5	223 s

3.6 Application to trajectory calculations

Running Lagrangian trajectory calculations is a particularly interesting test for assessing the impact of data compression on meteorological data because these trajectories are highly sensitive to small errors in winds and vertical velocities, allowing even subtle compression-induced distortions to accumulate and reveal their influence on atmospheric transport and dispersion patterns. We calculated trajectories using the ERA5 files compressed with the multiresolution-based grid adaptation as input files. We performed trajectory calculations for the test cases MRA_MW_2663 ($\mathrm{CR} = 1.9$), MRA_MW_3784 ($\mathrm{CR} = 3.1$),

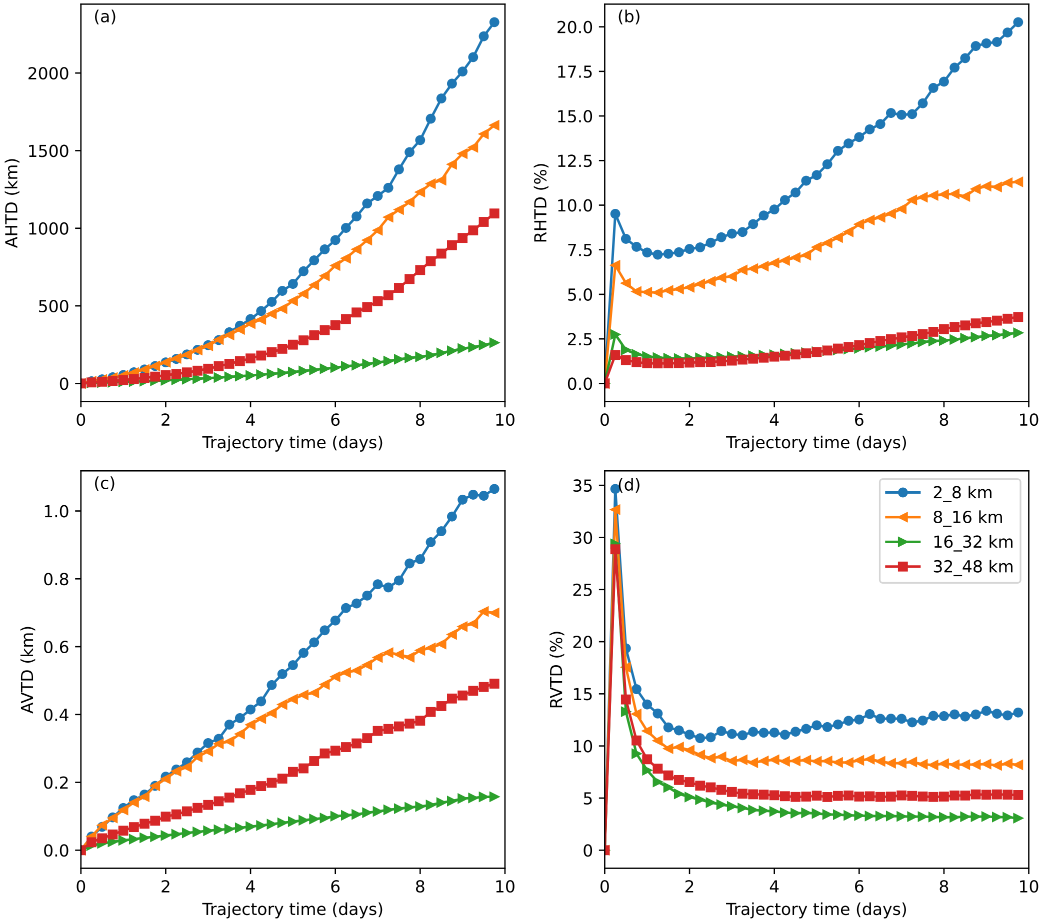

Figure 8. Absolute and relative vertical and horizontal transport deviations versus trajectory time for the 10-day forward trajectory calculations with MPTRAC using the meteorological reanalysis files compressed with the multiresolution-based grid adaptation for the test case MRA_MW_2663. The horizontal (a, c) and vertical (b, d) transport deviations have been separated into the altitude regions: 2–8 km, 8–16 km, 16–21 km and 32–48 km.

MRA_MW_3763 (CR = 4.5) and MRA_MW_3863 (CR = 12.7). Forward trajectories were calculated for 10 days starting on 1 January 2017. We used 10^4 air parcels that have been globally distributed over the altitude range of 2–48 km.

500 In Fig. 8 and Fig. 9 the absolute and relative horizontal and vertical transport deviations are shown for the test case with the highest accuracy (MRA_MW_3863) and the test case with the highest compression (MRA_MW_2663). The transport deviations have been separated into altitude regions of 2–8 km, 8–16 km, 16–32 km and 32–48 km and are a mean over all 10^4 trajectories, see Sect. 2.3.3. The highest horizontal and vertical transport deviations are found at the lowest altitude range of 2–8 km (free troposphere), while the lowest deviations are found at the altitude range of 16–32 km (lower stratosphere). 505 This is because more accurate trajectory calculations are possible since the stratosphere is stable stratified and the wind fields

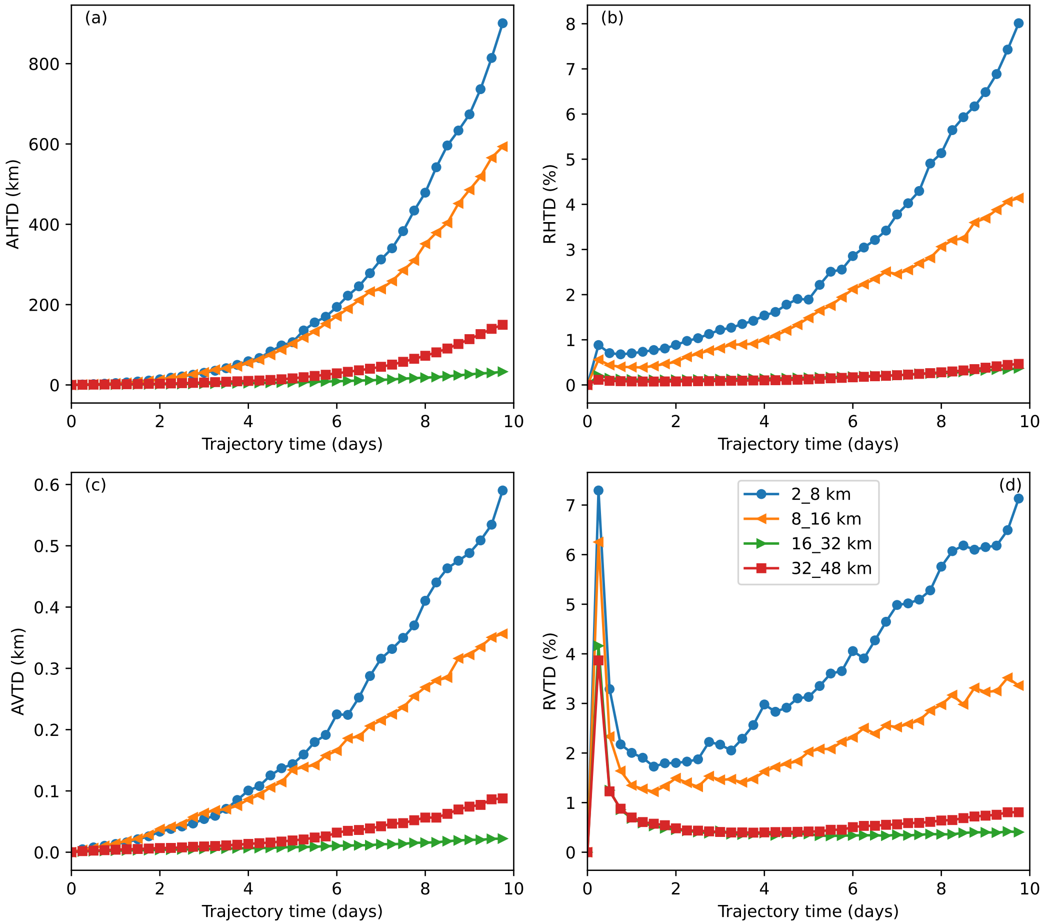

Figure 9. Same as Fig. 8, but for test case MRA_MW_3863.

are much smoother than in the troposphere. The troposphere is more dynamically variable which makes accurate trajectory calculation more challenging.

The transport deviations generally increase with trajectory time, reaching their respective horizontal and vertical maximum after 10 days. This development in time is typical for transport deviations, since trajectory calculations suffer from small local errors that accumulate over time (e.g. Kuo et al., 1985; Stohl, 1998; Harris et al., 2005; Engström and Magnusson, 2009). For the strong compression case (Fig. 8), the horizontal deviations are quite low at all considered altitude ranges for the first two days and then start to increase, reaching after 10 days 2300 km (20%) at 2–8 km, 1700 km at 8–16 km (10%), 250 km (2.5%) at 16–32 km and 1000 km at the altitude range 32–48 km (2.5%). In the vertical the transport deviations reach from 100 m for the altitude range 16–32 km (3%) to 1 km (13%) at the altitude range 2–8 km.

The horizontal and vertical transport deviations are significantly lower for the high accuracy case MRA_MW_3863 (Fig. 9). Deviations remain low for the first four days at all altitude regions considered and then start, as for the high compression case,

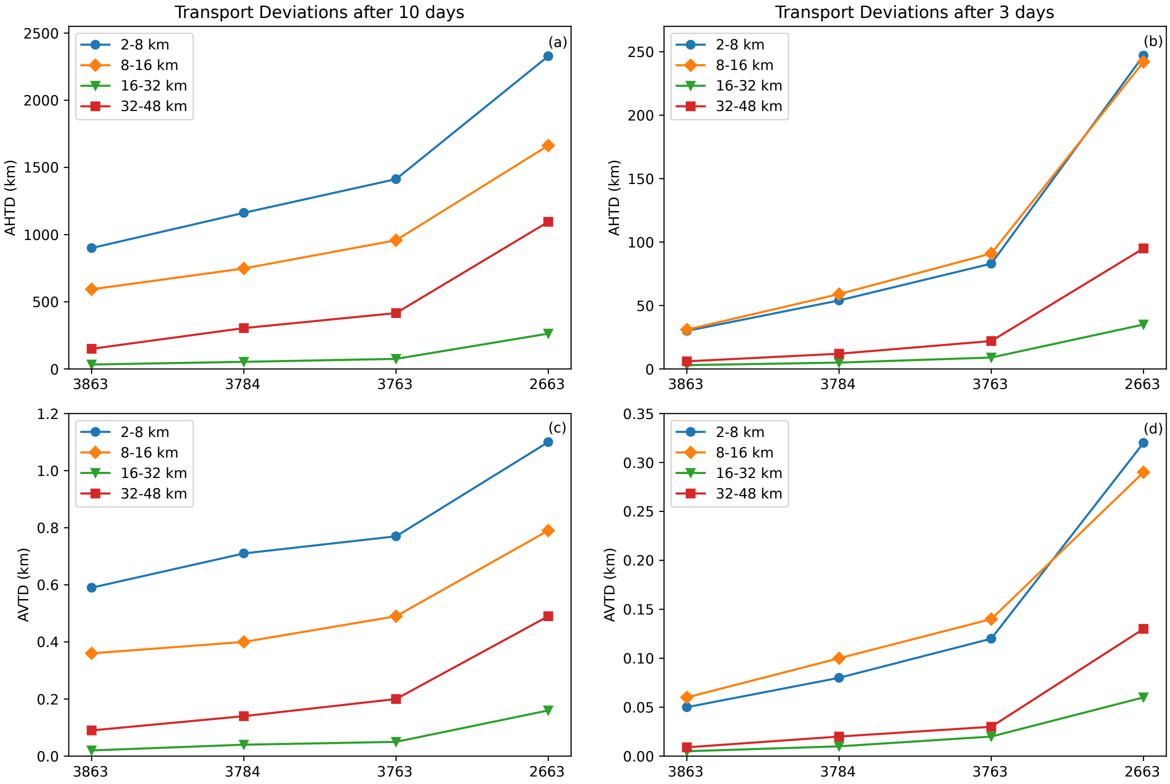

Figure 10. Absolute horizontal transport deviations versus compression ratio for the test cases MRA_MW_3863 ($\mathrm{CR} = 1.9$), MRA_MW_3784 ($\mathrm{CR} = 3.1$), MRA_MW_3763 ($\mathrm{CR} = 4.5$) and MRA_MW_2663 ($\mathrm{CR} = 12.6$). The left panels show the maximum absolute (a) horizontal (AHTD) and (c) vertical (AVTD) transport deviations after 10 days, the panels on the (b) horizontal and (d) vertical transport deviations after 3 days. Note the different y-scales for each panel.

to significantly increase, especially at the lowest altitude region. The horizontal deviations reach in this case to 900 km (8$\%$) at 2–8 km, 550 km at 8–16 km, 100 km at 32–48 km and 100 m at 16–32 km. In the vertical these reach up to 0.6 km (7$\%$) at 2–8 km, 0.35 km at 8–16 km, below 0.01 km at 16–32 km and 32–48 km.

Although these deviations seem to be large, these are in the range of transport deviations found in other studies. Rößler et al. (2018) compared six different numerical integration schemes and found that deviations were low for all schemes up to 5 days, but then began to rapidly increase for some schemes, resulting in horizontal transport deviations of up to 4400 km and vertical transport deviations of 4800 m. In Hoffmann et al. (2019) differences between trajectory simulations using ERA5 and ERA-Interim data were quantified. Using ERA5 for trajectory simulation transport deviations of up to 1400 km horizontally and 800 m vertically were found after 10 days due to parameterized diffusion and sub-grid scale wind fluctuations. These transport deviations were about a factor of 2 lower than using ERA-Interim for trajectory calculations. In another study by Hoffmann et al. (2022) absolute horizontal and vertical transport deviations were calculated in order to quantify the effects of simulated diffusion and sub-grid scale wind fluctuations on 8 day trajectories within the northern hemispheric jet stream. Different parameter choices for diffusion and sub-grid scale wind fluctuations were used. Depending on the parameter choice, horizontal transport deviations ranged from 100 km to about 1800 km and vertical transport deviations ranged from 100 m to 1 km after 8 days.

Comparing the transport deviations from Rößler et al. (2018); Hoffmann et al. (2019, 2022) with the ones derived in this study, we find that these lie in the typical range of transport deviations that can be expected when uncertainties from external sources are considered. Further, the largest deviations were found for the altitude region of 2–8 km after 10 days. For real case studies of trajectory calculations such a long duration would not be considered in the troposphere due to the dynamical variability and the according expected uncertainties of trajectory calculations in this region. In the troposphere trajectory calculations are usually performed up to a few days. For studies investigating e.g. air mass transport for pollutants, smoke or dust trajectory lengths of about 1–3 days are considered. In that time range the horizontal and vertical transport deviations are still reasonably low even for the high compression case MRA_MW_2663.

To better visualize this, in Fig. 10 the transport deviations reached after 10 days and after 3 days, respectively versus the compression test case are shown (ordered with an increasing compression ratio). Here, the test cases MRA_MW_3784 and MRA_MW_3763, for which we also calculated trajectories, are included. After 3 days transport deviations for the troposphere are approximately in the order of the ones found for the stratosphere after 10 days. This means that, even though the ERA5 data have been strongly compressed, the transport deviations for the trajectory length usually considered in the respective atmospheric regions are still tolerable. Note, we considered only pure advection here. If other processes are considered additionally, deviations may become even larger. Thus, a compromise between compression strength and remaining accuracy of the ERA5 data is always the best option.

3.7 Comparison to conventional compression methods

Figure 11 shows the maximum transport deviations of the trajectories after 10 days that we derived in this study alongside with trajectory deviations derived in a previous study where conventional compression methods were compared (Khosrawi and Hoffmann, 2025). The compression methods that were considered in our previous study were ZSTD, ZFP and PCK. ZFP was used with applying three different precision: 8, 12 and 16. As for Fig. 8-10 four altitude regions are considered: 2–8 km, 8–16 km, 16–32 km and 32–48 km.

In Fig. 11, the transport deviations are sorted by increasing compression ratio. The lowest compression ratio (CR $= 1.5$) was derived with the lossless compressor ZSTD, the highest (CR $= 25$) using the lossy compressor ZFP with a precision of 8. Our compression test MRA_MW_3863 lies with a compression ratio of 1.9 between the compression ratio of ZSTD and PCK, but transport deviations are higher for the troposphere and the upper stratosphere (up to 900 km compared to 0 km or up to 40 km for ZSTD and PCK, respectively). In the lower stratosphere (16–32 km) transport deviations are low for all three compressions and approximately of the same order.

Compression tests, MRA_MW_3784 and MRA_MW_3763, with compression ratios of 3.1 and 4.5, respectively, lie between PCK (CR $= 2$) and ZFP16 (CR $= 7$). Higher transport deviations are also found here in the troposphere and upper stratosphere,

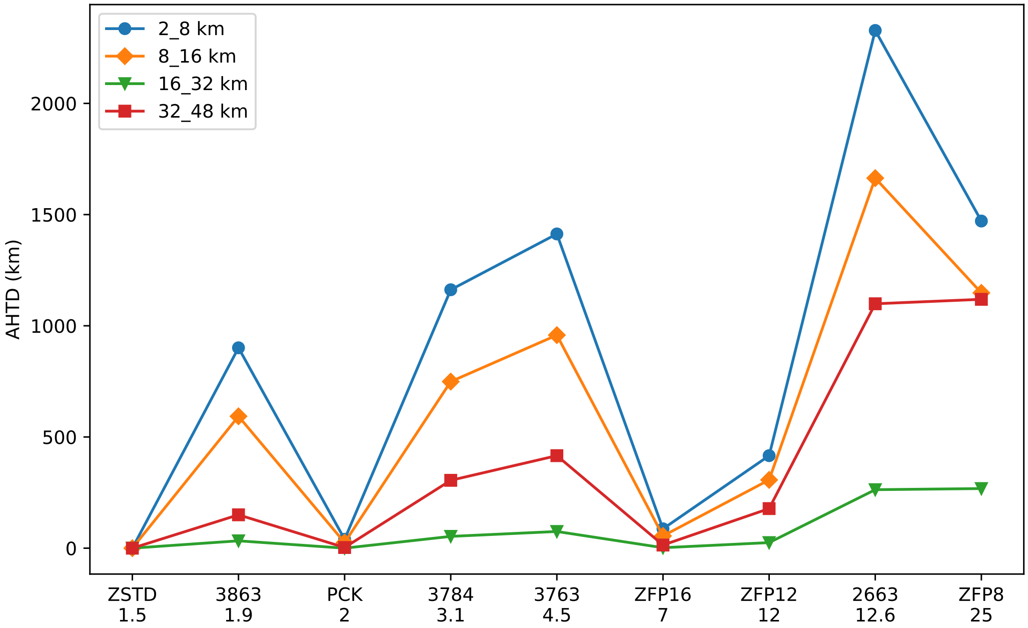

Figure 11. Absolute horizontal transport deviations after 10 days versus compression ratio for the MRA_MW test cases shown in Fig. 10, MRA_MW_3863 (CR $= 1.9$), MRA_MW_3784 (CR $= 3.1$), MRA_MW_3763 (CR $= 4.5$) and MRA_MW_2663 (CR $= 12.6$), in comparison to the conventional compression methods PCK (CR $= 2$) and ZFP (CR $= 7, 12$ and 25).

but not in the lower stratosphere. Our compression test (MRA_MW_2663) with the strongest compression with a compression ratio of 12.6 is approximately in the order that was derived with ZFP12. However, also here transport deviations are larger for MRA_MW_2663 for all altitude regions considered.

Thus, this comparison shows that with the presented test case compression ratios as with advanced compression methods can be achieved, however currently more lossy since the transport deviations of the trajectories calculated with MRA_MW compressed files are larger. However, as discussed in Sect. 3.6, these deviations are nevertheless within the range of deviations that can be expected when uncertainties from external sources are considered (Rößler et al., 2018; Hoffmann et al., 2019, 2022).

4 Conclusions

In order to be prepared for the upcoming ERA6 data and to be able to cope with the high storage requirements that come with this data set, data compression is a promising solution. In this study we demonstrated a proof of concept for applying multiresolution-based grid adaptation as a lossy data compression method. Thereby, a multi-scale decompostion represents the data at successive levels of refinement, with localized detail coefficients quantifying differences between scales. When the differences are small, the data ca be projected onto a coarser grid without significant loss of information. Building on this principle, an adaptive representation is constructed that preserves a prescribed accuracy while reducing the number of degrees of freedom. Storing the data in this adaptive multi-scale form yields in effective data compression.

Data compression based on multiresolution-based grid adaptation is here performed by using the MRA-MW library. A library which has been derived from the first-order hyperbolic partial differential equation (PDE) solver MultiWave (https://www.igpm.rwth-aachen.de/forschung/multiwave). The primary objective of the MRA-MW library is to provide an easy-to-use C interface to MultiWave's grid adaptation module. In this study, the MRA-MW library has been successfully coupled to MPTRAC. By using MRA-MW within MPTRAC, the user can easily adjust the compression strength and accuracy of the resulting compression of the data files by adjusting the dimension of the DG space p (`PDIM`), the maximum refinement level L (`max_level`) and by adjusting the parameters `Nd0_x` and `Nd0_y` that define the inital grid. Using the MPTRAC module `met_conv` ten test cases have been conducted using a `PDIM` of 2 and 3, a maximum level of refinement `max_level` of 6, 7 and 8 and `Nd0_x` and `Nd0_y` of 4 and 2, 6 and 3 and 8 and 4.

In these test cases compression ratios (CRs) ranging from 1.6 to 12.6 were achieved. Although high compression ratios can be generally achieved, maintaining a very high accuracy (correlation coefficient of $r_{\text{min}} \geq 0.99999$) limits the CR currently to around 1.6–1.9. However, to overcome this and to achieve higher compression ratios while at the same time maintaining a sufficient accuracy, we combined the compression with MRA-MW with the lossless compressor ZSTD. Compression ratios of 2.2 to 16.4 were attained, which corresponds to an additional reduction in file size of up to about 30%. Note, maintaining a high accuracy as of $r \geq 0.99999$ corresponds to a near lossless compression, thus it is not astonishing that with keeping that limit compression ratios are not that high, since also lossless compression methods rarely do exceed a compression ratio of 1.5 (Lindstrom, 2014). The presented method is a lossy compression method, thus a certain amount of loss needs to be allowed. Important is how much loss is tolerable. To assess this, we also performed 10-day forward trajectory calculations using the compressed ERA5 data files as input files.

The trajectory calculations showed that an increasing compression strength and thus a decreasing correlation results in larger transport deviations, especially for the lowest considered altitude region (2–8 km), with deviations ranging from 900 km up to 2500 km after 10 days. Nevertheless, although these deviations are larger than those found when using conventional compression methods, they are comparable to those found in other studies and are in the range of deviations that can be expected when uncertainties from external sources are considered (Rößler et al., 2018; Hoffmann et al., 2019, 2022).

Future work will focus on optimizing the multiresolution-based grid adaptation compression method to further improve compression efficiency while maintaining at the same time a high accuracy and on the application to the upcoming ERA6 data and on the compression of satellite data. Further, we plan to exploit the full potential of the multi-scale based data analysis and use the provided functions to directly run trajectory calculation. This will eliminate the need to first decompress and interpolate the data back onto a Cartesian grid for trajectory calculations. This will make both data storage and trajectory calculations more efficient.

Appendix A: Proof of Pearson estimates

Here we derive a strategy for the choice of the thresholding value $\varepsilon_{\max}$ to generate a given Pearson correlation coefficient $\rho_{\min}$. For this purpose, we introduce the *Pearson correlation coefficient* for some uniformly distributed random variables $X,Y \sim \mathcal{U}([0,1]^2)$ by

$$\rho(X,Y) := \frac{\mathrm{Cov}(X,Y)}{\sqrt{\mathrm{Var}[X]}\cdot\sqrt{\mathrm{Var}[Y]}} \equiv \frac{\mathbb{E}[X-\mathbb{E}[X]]\cdot\mathbb{E}[Y-\mathbb{E}[Y]]}{\sqrt{\mathrm{Var}[X]}\cdot\sqrt{\mathrm{Var}[Y]}}. \tag{A1}$$

Lemma 1 (Control of Pearson Correlation Coefficient)**.**

Let $u^L \in S_L$, as defined in equation (2)*, be the projection of u onto S_L and let $u^{L,\varepsilon}$ denote its sparse approximation* (10)*. Let the minimum correlation coefficient $\rho_{min} \in [0,1]$ be fixed. By choosing the threshold value $\varepsilon_{max} \geq 0$ such that*

$$\varepsilon_{max} \leq \frac{\mathrm{Var}[u^L]\,(1-\rho_{min})}{C\,(1+\rho_{min})}, \tag{A2}$$

it holds $\rho(u^L, u^{L,\varepsilon}) \geq \rho_{min}$, where $C > 0$ is defined as in Theorem 1.

Proof. Let $\overline{u^L} := \mathbb{E}[u^L] = \int_\Omega u^L \,\mathrm{d}x$ and $\overline{u^{L,\varepsilon}} := \mathbb{E}[u^{L,\varepsilon}] = \int_\Omega u^{L,\varepsilon}\,\mathrm{d}x$ denote the expectation of the projected function u^L and the sparse approximation $u^{L,\varepsilon}$, respectively. Using the multi-scale representation of the sparse approximation we have

$$\overline{u^L} = \overline{u^{L,\varepsilon}}, \tag{A3}$$

as shown in Gerhard (2017, Conclusion 3.3). Using (A3) it holds

$$u^{L,\varepsilon} - \overline{u^{L,\varepsilon}} = u^L - \overline{u^L} - \left(u^L - u^{L,\varepsilon}\right).$$

Thus, by applying Hölder's inequality, we estimate the covariance as follows:

$$\begin{aligned}
\mathrm{Cov}(u^L, u^{L,\varepsilon}) &= \mathbb{E}\left[\left(u^L - \overline{u^L}\right)\left(u^{L,\varepsilon} - \overline{u^{L,\varepsilon}}\right)\right] = \mathbb{E}\left[\left(u^L - \overline{u^L}\right)\left(u^L - \overline{u^L} - \left(u^L - u^{L,\varepsilon}\right)\right)\right] \\
&= \mathbb{E}\left[\left(u^L - \overline{u^L}\right)^2\right] - \mathbb{E}\left[\left(u^L - \overline{u^L}\right)\cdot\left(u^L - u^{L,\varepsilon}\right)\right] \\
&\geq \mathbb{E}\left[\left(u^L - \overline{u^L}\right)^2\right] - \mathbb{E}\left[\left|u^L - \overline{u^L}\right|\cdot\left|u^L - u^{L,\varepsilon}\right|\right] \\
&\geq \mathbb{E}\left[\left(u^L - \overline{u^L}\right)^2\right] - \sqrt{\mathbb{E}\left[\left|u^L - \overline{u^L}\right|^2\right]}\cdot\sqrt{\mathbb{E}\left[\left|u^L - u^{L,\varepsilon}\right|^2\right]}.
\end{aligned}$$

Since $\sqrt{\mathbb{E}\left[|u^L - u^{L,\varepsilon}|^2\right]} = \|u^L - u^{L,\varepsilon}\|_{L^2(\Omega)}$ we can apply Theorem 1 to obtain a lower bound for the covariance:

$$\mathrm{Cov}(u^L, u^{L,\varepsilon}) \geq \mathbb{E}\left[\left(u^L - \overline{u^L}\right)^2\right] - C\cdot\varepsilon_{\max} = \mathrm{Var}\left[u^L\right] - \sqrt{\mathrm{Var}\left[u^L\right]}\cdot C\cdot\varepsilon_{\max}. \tag{A4}$$

By applying (A3) along with the Minkowski inequality, we derive an estimate for the variance of the sparse approximation:

$$\begin{aligned}
\sqrt{\mathrm{Var}[u^{L,\varepsilon}]} &= \sqrt{\mathbb{E}\left[\left(u^{L,\varepsilon} - \overline{u^{L,\varepsilon}}\right)^2\right]} = \sqrt{\mathbb{E}\left[\left(u^{L,\varepsilon} - \overline{u^L}\right)^2\right]} = \sqrt{\mathbb{E}\left[\left(u^{L,\varepsilon} - u^L + u^L - \overline{u^L}\right)^2\right]} \\
&\leq \sqrt{\mathbb{E}\left[\left(u^{L,\varepsilon} - u^L\right)^2\right]} + \sqrt{\mathbb{E}\left[\left(u^L - \overline{u^L}\right)^2\right]}.
\end{aligned}$$

Applying the thresholding error (8) in Theorem 1 yields

$$\sqrt{\mathrm{Var}[u^{L,\varepsilon}]} \leq C \cdot \varepsilon_{\text{max}} + \sqrt{\mathbb{E}\left[\left(u^L - \overline{u^L}\right)^2\right]} = C \cdot \varepsilon_{\text{max}} + \sqrt{\mathrm{Var}\left[u^L\right]}. \tag{A5}$$

Given $\rho_{\text{min}} > 0$, we apply the estimates (A4) and (A5) to the correlation coefficient defined in (A1). This results in the following inequality:

$$\rho(u^L, u^{L,\varepsilon}) \geq \frac{\mathrm{Var}\left[u^L\right] - \sqrt{\mathrm{Var}\left[u^L\right]} \cdot C \cdot \varepsilon_{\text{max}}}{\sqrt{\mathrm{Var}[u^L]}\left(C \cdot \varepsilon_{\text{max}} + \sqrt{\mathrm{Var}\left[u^L\right]}\right)} \geq \rho_{\text{min}}. \tag{A6}$$

Rearranging the terms in (A6) yields (A2).

□

Code and data availability. MPTRAC is made available under the terms and conditions of the GNU General Public License (GPL) version 3. The current and former versions of MPTRAC can be downloaded at https://github.com/slcs-jsc/mptrac (Hoffmann et al., 2016, 2022, 2025). MRA-MW can be downloaded at https://git-ce.rwth-aachen.de/igpm/mra-mw. The ERA5 data can be obtained from the European Centre for Medium-Range Weather Forecasts (ECMWF) Meteorological Archival and Retrieval System (MARS), see https://www.ecmwf.int/en/forecasts/datasets (Hersbach et al., 2020). The code and data for this study will be published on Zenodo.

Author contribuzion. FK, LH, AK, SM designed the study. AK wrote the MRA-MW C interface. LH coupled MRA-MW with MPTRAC. FK performed the data analysis, testing and evaluating the compression and calculating the trajectories. FK and AK wrote the manuscript with input from LH and SM.

Competing interests. Lars Hoffmann is an editor at Geoscientific Model Development. Otherwise, the authors declare that they have no competing interests

Acknowledgements. The work presented in this paper was funded by the BMFTR project ADAPTEX (FKZ: 16ME0670). We acknowledge the Jülich Supercomputing Centre for providing computing time and storage resources on the JUWELS supercomputer.

References

Baker, A. H., Hammerling, D. M., Mickelson, S. A., Xu, H., Stolpe, M. B., Naveau, P., Sanderson, B., Ebert-Uphoff, I., Samarasinghe, S., De Simone, F., Carbone, F., Gencarelli, C. N., Dennis, J. M., Kay, J. E., and Lindstrom, P.: Evaluating lossy data compression on climate simulation data within a large ensemble, Geosci. Model Dev., 9, 4381–4403, https://doi.org/10.5194/gmd-9-4381-2016, 2016.

Böing, N., Holke, J., Hergl, C., Spataro, L., Gassner, G., and Basermann, A.: Lossy Data Compression By Adaptive Mesh Coarsening, https://doi.org/10.48550/arXiv.2407.17316, 2024.

Chen, Y., Simon, K., and Behrens, J.: Extending legacy climate models by adaptive mesh refinement for single-component tracer transport: a case study with ECHAM6.3-HAM2.3-MOZ1.0, Geosci. Model Dev., 14, 2289–2316, https://doi.org/10.5194/gmd-14-2289-2021, 2021.

Delaunay, X., Courtois, A., and Gouillon, F.: Evaluation of lossless and lossy algorithms for the compression of scientific datasets in netCDF-4 or HDF5 files, Geosci. Model Dev., 12, 4099–4113, https://doi.org/10.5194/gmd-12-4099-2019, 2019.

Di, S. and Cappello, F.: Fast Error-Bounded Lossy HPC Data Compression with SZ, in: 2016 IEEE International Parallel and Distributed Processing Symposium (IPDPS), https://doi.org/10.1109/IPDPS.2016.11, 2016.

Duwe, K., Lüttgau, J., Mania, G., Squar, J., Fuchs, A., Kuhn, M., Betke, E., and Ludwig, T.: State of the art and future trends in data reduction for high-performance computing, Supercomp. Front. Inn., 7, https://doi.org/10.14529/jsfi200101, 2020.

Engström, A. and Magnusson, L.: Estimating trajectory uncertainties due to flow dependent errors in the atmospheric analysis, Atmos. Chem. Phys., 9, 8857–8867, https://doi.org/10.5194/acp-9-8857-2009, 2009.

Garcia-Menendez, F. and Odman, M. T.: Adaptive grid use in air quality modeling, Atmosphere, 2, 484–509, https://doi.org/10.3390/atmos203484, 2011.

Gerhard, N.: An Adaptive Multiresolution Discontinuous Galerkin Scheme for Conservation Laws, Ph.D. thesis, RWTH Aachen University, https://doi.org/10.18154/RWTH-2017-06869, 2017.

Gerhard, N. and Müller, S.: Adaptive multiresolution discontinuous Galerkin schemes for conservation laws: multi-dimensional case, Comp. Appl. Math, 35, 321–349, https://doi.org/10.1007/s40314-014-0134-y, 2016.

Gerhard, N., Iacono, F., May, G., Müller, S., and Schäfer, R.: A High-Order Discontinuous Galerkin Discretization with Multiwavelet-Based Grid Adaptation for Compressible Flows, J. Sci. Comput., 62, 25–52, https://doi.org/10.1007/s10915-014-9846-9, 2015.

Gerwig, E., Hort, M., Behrens, J., and Langmann, B.: An adaptive semi-Lagrangian advection model for transport of volcanic emissions in the atmosphere, Nat. Hazards Earth Syst. Sci, 18, https://doi.org/10.5194/nhess-18-1517-2018, 2018.

Gottschlich-Müller, B. and Müller, S.: On multi-scale concepts for multi-dimensional conservation laws, in: Numerical Treatment of Multi-Scale Problems (Proceedings of the 13th GAMM-Seminar, Kiel, Jan. 24 - 26, 1997, edited by Hackbusch, W. and Wittum, G., vol. 70, pp. 119–133, Vieweg-Verlag, Braunschweig, ISBN 3528031204, 1999.

Harris, J. M., Drexler, R. R., and Oltmans, S. J.: Trajectory model sensitivity to differences in input data and vertical transport method, J. Geophys. Res., 110, D14 109, https://doi.org/10.1029/2004JD005750, 2005.

Harten, A.: Discrete multi-resolution analysis and generalized wavelets, Applied Numer. Math., 12, 153–192, https://doi.org/10.1016/0168-9274(93)90117-A, 1993.

Harten, A.: Multiresolution Representation of Data: A General Framework, SIAM Journal on Numerical Analysis, 33, 1205–1256, http://www.jstor.org/stable/2158503, 1996.

Hersbach, H., Bell, B., Berrisford, P., Hirahara, S., Horányi, A., Muñoz Sabater, J., Nicolas, J., Peubey, C., Radu, R., Schepers, D., Simmons, A., Soci, C., Abdalla, S., Abellan, X., Balsamo, G., Bechtold, P., Biavati, G., Bidlot, J., Bonavita, M., De Chiara, G., Dahlgren, P., Dee, D., Diamantakis, M., Dragani, R., Flemming, J., Forbes, R., Fuentes, M., Geer, A., Haimberger, L., Healy, S., Hogan, R. J., Hólm, E., Janisková, M., Keeley, S., Laloyaux, P., Lopez, P., Lupu, C., Radnoti, G., de Rosnay, P., Rozum, I., Vamborg, F., Villaume, S., and Thépaut, J.-N.: The ERA5 global reanalysis, Q. J. Roy. Meteor. Soc., 146, 1999–2049, https://doi.org/10.1002/qj.3803, 2020.

Hoffmann, L., Rößler, T., Griessbach, S., Heng, Y., and Stein, O.: Lagrangian transport simulations of volcanic sulfur dioxide emissions: impact of meteorological data products, J. Geophys. Res., 121, 4651–4673, https://doi.org/10.1002/2015JD023749, 2016.

Hoffmann, L., Hertzog, A., Rößler, T., Stein, O., and Wu, X.: Intercomparison of meteorological analyses and trajectories in the Antarctic lower stratosphere with Concordiasi superpressure balloon observations, Atmos. Chem. Phys., 17, 8045–8061, https://doi.org/10.5194/acp-17-8045-2017, 2017.

Hoffmann, L., Günther, G., Li, D., Stein, O., Wu, X., Griessbach, S., Heng, Y., Konopka, P., Müller, R., Vogel, B., and Wright, J. S.: From ERA-Interim to ERA5: the considerable impact of ECMWF's next-generation reanalysis on Lagrangian transport simulations, Atmos. Chem. Phys., 19, 3097–3124, https://doi.org/10.5194/acp-19-3097-2019, 2019.

Hoffmann, L., Baumeister, P. F., Cai, Z., Clemens, J., Griessbach, S., Günther, G., Heng, Y., Liu, M., Haghighi Mood, K., Stein, O., Thomas, N., Vogel, B., Wu, X., and Zou, L.: Massive-Parallel Trajectory Calculations version 2.2 (MPTRAC-2.2): Lagrangian transport simulations on graphics processing units (GPUs), Geosci. Model Dev., 15, 2731–2762, https://doi.org/10.5194/gmd-15-2731-2022, 2022.

Hoffmann, L., Clemens, J., Griessbach, S., Haghighi Mood, K., Heng, Y., Khosrawi, F., Liu, M., Lu, Y.-S., Meyer, C., Nobre Wittwer, N., Wu, X., and Zou, L.: MPTRAC: A high-performance Lagrangian transport model for atmospheric air parcel dispersion, J. Open Source Softw., 10, 8177, https://doi.org/10.21105/joss.08177, 2025.

Huang, L. and Hoefler, T.: Compressing multidimensional weather and cliamte data into neural networks, https://doi.org/https://doi.org/10.48550/arXiv.2210.12538, 2023.

Hübbe, N., Wegener, A., Kunkel, J. M., Ling, Y., and Ludwig, T.: Evaluating Lossy Compression on Climate Data, in: Supercomputing, edited by Kunkel, J. M., Ludwig, T., and Meuer, H. W., pp. 343–356, Springer Berlin Heidelberg, Berlin, Heidelberg, https://doi.org/10.1007/978-3-642-38750-0_26, 2013.

Jablonowski, C., Oehmke, R. C., and Stout, W. F.: Block-structured adaptive meshes and reduced grids for atmospheric general circulation models, Phil. Trans. R. Soc., 367, 4497–4522, https://doi.org/10.1008/rsta.2009.01500, 2009.

Khosrawi, F. and Hoffmann, L.: Compression of ERA5 meteorological reanalysis data and their application to simulations with the Lagrangian model for Massive Parallel Trajectory Calculations (MPTRAC v2.7), EGUsphere [preprint], https://doi.org/https://doi.org/10.5194/egusphere-2025-3147, 2025.

Klöwer, M., Razinger, M., Dominguez, J. J., Düben, P. D., and Palmer, T. N.: Compressing atmospheric data into its real information content, Nature Comp. Sci., 1, 713–724, https://doi.org/10.1038/s43588-021-00156-2, 2021.

Kuo, Y.-H., Skumanich, M., Haagenson, P. L., and Chang, J. S.: The accuracy of trajectory models as revealed by the observing system simulation experiments, Mon. Weather Rev., 113, 1852–1867, https://doi.org/10.1175/1520-0493(1985)113<1852:TAOTMA>2.0.CO;2, 1985.

Lindstrom, P.: Fixed-rate compressed floating-point arrays, in: IEEE Transactions on Visualization and Computer Graphics, vol. 20 (12), pp. 2674–2683, https://doi.org/10.1109/TVCG.2014.2346458, 2014.

Liu, M., Hoffmann, L., Griessbach, S., Cai, Z., Heng, Y., and Wu, X.: Improved representation of volcanic sulfur dioxide depletion in Lagrangian transport simulations: a case study with MPTRAC v2.4, Geosci. Model Dev., 16, 5197–5217, https://doi.org/10.5194/gmd-16-5197-2023, 2023.

Liu, Q., Gong, B., Zhuang, X., Zhong, X., Kang, Z., and Li, H.: Compressing high-resolution data through latent representation encoding for downscaling large-scale AI weather forecast model, EGUsphere [preprint], https://doi.org/10.5194/egusphere-2024-3183, 2024.

Poppick, A., Nardi, J., Feldmann, N., Baker, A., Pinard, A., and Hammerling, D. M.: A statistical analysis of lossily compressed climate model data, Comput. Geosc., 145, 104 599, https://doi.org/10.1016/j.cageo.2020.104599, 2020.

Rolph, G. D. and Draxler, R. R.: Sensitivity of three-dimensional trajectories to the spatial and temporal densities of the wind field, J. Appl. Meteorol., 29, 1043–1054, 1990.

Rößler, T., Stein, O., Heng, Y., Baumeister, P., and Hoffmann, L.: Trajectory errors of different numerical integration schemes diagnosed with the MPTRAC advection module driven by ECMWF operational analyses, Geosci. Model Dev., 11, 575–592, https://doi.org/10.5194/gmd-11-575-2018, 2018.

Silver, J. D. and Zender, C. S.: The compression–error trade-off for large gridded data sets, Geosci. Model Dev., 10, 413–423, https://doi.org/10.5194/gmd-10-413-2017, 2017.

Stohl, A.: Computation, accuracy and applications of trajectories – a review and bibliography, Atmos. Environ., 32, 947–966, https://doi.org/10.1016/S1352-2310(97)00457-3, 1998.

Tao, D., Di, S., Chen, Z., and Cappello, F.: Significantly Improving Lossy Compression for Scientific Data Sets Based on Multidimensional Prediction and Error-Controlled Quantization, https://doi.org/10.48550/arXiv.1706.03791, 2017.

Tao, D., Di, S., Guo, H., Z., C., and Cappello, F.: Z-checker: A framework for assessing lossy compression of scientific data, The International Journal of High Performance Computing Applications, 33(2), 285–303, https://doi.org/10.1177/1094342017737147, 2019.

Tintó Prims, O., Redl, R., Rautenhaus, M., Selz, T., Matsunobu, T., Modali, K. R., and Craig, G.: The effect of lossy compression of numerical weather prediction data on data analysis: a case study using enstools-compression 2023.11, Geosci. Model Dev., 17, 8909–8925, https://doi.org/10.5194/gmd-17-8909-2024, 2024.

Walters, M. S. and Wong, D. C.: The impact of altering emission data precision on compression efficiency and accuracy of simulations of the community multiscale air quality model, Geosci. Model Dev., 16, 1179–1190, https://doi.org/10.5194/gmd-16-1179-2023, 2023.

Wegener, A.: Universal numerical encoder and profiler reduces computing's memory wall with software, FPGA, and SoC implementations, arXiv, https://doi.org/https://arxiv.org/abs/1303.4994, 2013.

World Meteorological Organization: WMO Manual on Codes, International Codes, Volume I.2: Part B – Binary Codes (FM 92-XIV GRIB), 2025 edn., https://community.wmo.int/about-manual-codes-volume-i2, latest print edition of the GRIB specification, 2025.

Zender, C. S.: Bit Grooming: statistically accurate precision-preserving quantization with compression, evaluated in the netCDF Operators (NCO, v4.4.8+), Geosci. Model Dev., 9, 3199–3211, https://doi.org/10.5194/gmd-9-3199-2016, 2016.